HF radar observations of surface circulation off Bodega Bay (northern California, USA)

David M. Kaplan
Wildlife, Fish and Conservation Biology, University of California, Davis, Davis, California, USA

John Largier
Bodega Marine Laboratory, University of California, Davis, Bodega, California, USA

Louis W. Botsford
Wildlife, Fish and Conservation Biology, University of California, Davis, Davis, California, USA

Received 16 March 2005; revised 7 June 2005; accepted 29 June 2005; published 18 October 2005.

[1] Two high-frequency radar stations (CODAR) were installed along the northern California coast in May 2001. Comparisons of radar data with acoustic Doppler current profiler (ADCP) current data and near-surface drifter tracks indicate considerable agreement, with minimum RMS differences of order 0.05–0.15 m/s and average drifter-HF-radar track separation rates of 5 ± 3 km/d. Radar data resolve the three main sources of intraseasonal current variability in the area: (1) upwelling/relaxation dynamics, (2) tidal and diurnal forcing, and (3) inertial currents. Subtidal fluctuations are the largest component of variability, accounting for 45–75% of the variance. Wind-driven dynamics are the dominant source of this subtidal variability (67% of subtidal variability). Both upwelling and relaxation periods exhibit consistent patterns of surface velocity, with nearshore currents being slower and more poleward than offshore currents, which are strongly equatorward. Analysis of tidal and inertial variability indicate that current fluctuations are polarized toward clockwise rotation and are generally weaker and more linearly polarized near the coast. M_2 tidal current ellipses switch direction of rotation at the shelf break, suggesting the presence of internal tidal waves. Currents in all frequency bands are deflected and accelerated around Pt. Reyes, and there are indications of increased current variability and changes in flow direction near Cordell Bank. The presence of considerable cross-shore and alongshore gradients in the strength and direction of surface flow patterns, and in particular weak poleward currents over the inner shelf, could have important consequences for plankton retention in the area.

Citation: Kaplan, D. M., J. Largier, and L. W. Botsford (2005), HF radar observations of surface circulation off Bodega Bay (northern California, USA), *J. Geophys. Res.*, *110*, C10020, doi:10.1029/2005JC002959.

1. Introduction

[2] The circulation off northern California has been well studied previously and much of the fundamental understanding of wind forcing and coastal upwelling has emerged from studies conducted between Point Reyes and Point Arena (Figure 1). This region has been the focus of several important oceanographic programs: CODE [*Beardsley and Lentz*, 1987], CTZ [*Brink and Cowles*, 1991], NCCCS [*Largier et al.*, 1993], SMILE [*Dever*, 1997a], STRESS [*Trowbridge and Lentz*, 1998], and most recently WEST (J. L. Largier et al., WEST: A northern California study of the role of wind driven transport on productivity of coastal plankton communities, submitted to *Deep-Sea Research, Part II*, 2005).

0148-0227/05/2005JC002959$09.00

[3] The Coastal Ocean Dynamics Experiment (CODE) in the early 1980s described many of the fundamental characteristics of ocean currents in the area and provided an in-depth analysis of the alongshore momentum balance. The observed upwelling of cold waters along the coast was related to both local wind forcing [*Winant et al.*, 1987] and remote forcing via coastally trapped waves [*Denbo and Allen*, 1987]. The presence of a strong and persistent upwelling center immediately south of Pt. Arena was recognized [*Huyer and Kosro*, 1987], as was the tendency for an annual maximum in upwelling during spring and early summer [*Strub et al.*, 1987]. South of the upwelling center, strong fluctuations in currents and vertical structure were observed in response to fluctuations in wind forcing. Most notably, poleward flows (i.e., flows toward the north in the northern hemisphere) and warmer waters were observed nearshore during periods in which equatorward (i.e., toward the south) wind forcing relaxed [*Send et al.*,

1987; *Huyer and Kosro*, 1987; *Davis*, 1985; *Kosro*, 1987]. Many of these results were confirmed during NCCCS, with similar results being obtained at locations further north along the Californian coast. Alongshore variability was described [*Largier et al.*, 1993; *Bray and Greengrove*, 1993], pointing to the strength of upwelling at headlands (e.g., Pt. Arena, Cape Mendocino) and the occurrence of nearshore poleward flow and stratification between headlands (e.g., Bodega, Fort Bragg). During CTZ, concurrent with NCCCS, the importance of offshore forcing of the shelf circulation by mesoscale eddies came to be well appreciated [*Washburn et al.*, 1991; *Largier et al.*, 1993]. Studies during SMILE resolved the surface boundary layer and the relationship between near-surface stratification, wind forcing and Ekman transport [*Dever*, 1997b; *Lentz*, 1994].

[4] As part of the Wind Events and Shelf Transport program (WEST), fieldwork was conducted from 2000 to 2003 to study the role of wind-driven transport in primary and secondary productivity over the shelf. While CODE, NCCCS and SMILE yielded a detailed understanding of the response of the alongshore current to wind forcing, the response of the cross-shore current remained poorly understood and the spatial pattern of shelf flow was sparsely sampled so that transport pathways were poorly defined. The first of these challenges is addressed by *Dever et al.* [2005], who describe the results from a mooring array designed to determine the response of cross-shore currents to wind forcing. In this paper we address the second challenge, reporting results from the HF radar system (CODAR), which was installed during WEST to monitor surface circulation over an extensive area of the shelf off Bodega-Reyes.

[5] The biological importance of circulation in this area, and specifically poleward flows during relaxation, became clear through the work of *Wing et al.* [1995a, 1995b, 1998a, 1998b] on meroplankton. To the south of the Pt. Reyes lies Drakes Bay (Figure 1), a relatively protected area that has been associated with higher temperatures, low-salinity outflow from San Fransisco Bay and the apparent retention of planktonic larvae [*Wing et al.*, 1998b]. During relaxation periods, there is evidence of warmer water moving along the coast around Point Reyes and into and past Bodega Bay [*Send et al.*, 1987; *Wing et al.*, 1995a, 1995b; M. Roughan et al., Subsurface recirculation and larval retention in the lee of a small headland: A variation on the upwelling shadow theme, submitted to *Journal of Geophysical Research*, 2005]. These relaxation events result in increased settlement of invertebrate larvae at Bodega Head [*Wing et al.*, 1998a] and in Bodega Bay [*Mace*, 2005]. The biological importance of these mechanisms is that they provide a way for larvae to maintain alongshore position in the presence of equatorward flows, which is a necessary characteristic for population persistence [*Gaylord and Gaines*, 2000; *Largier*, 2003]. Coastal flow patterns and relaxation events are also likely to be important for primary productivity over the shelf as they affect shelf residence times and nutrient availability (L. W. Botsford et al., Dynamic effects of variable winds on biological productivity in coastal upwelling systems with advective losses, submitted to *Deep-Sea Research, Part II*, 2005).

[6] So, while prior studies have provided an understanding of the response of shelf waters to equatorward wind forcing and indicated the importance of poleward flow events and larval retention for planktonic dispersal, neither the spatial form of observed flows nor the spatial structure of high-frequency motions (e.g., tides) have been properly described for this region. To better understand transport in coastal upwelling regions, and hence primary productivity and the persistence of meroplanktonic species on the shelf in coastal upwelling regions, two Coastal Ocean Dynamics Applications Radar (CODAR) systems were installed along the coast of northern California at Point Reyes and Bodega Head in May 2001 (and a third unit was added at Gerstle Cove in May 2002). These systems have operated nearly continuously since that time and have given us an unprecedented view of surface currents in an upwelling-dominated region.

[7] In this study, we examine high-frequency (HF) radar data from two radar units during 2001, exploring the different modes of variability in surface currents in the area. We begin by examining general patterns of surface circulation (section 3). There is significant cross-shore structure in alongshore flows in the area, with stronger, more equatorward flows offshore and weak or poleward mean flow over the mid- and inner shelf (section 3.1). Within 15 km of shore, poleward currents can exceed 0.2 m/s and strong equatorward flow is rare (section 3.2). Comparisons of HF radar data with colocated acoustic Doppler current profiler (ADCP) and drifter data reveal a high degree of agreement (section 4), though significant differences are observed associated with the vertical penetration of surface wind forcing (section 4.1) and periods of weakening of upwelling conditions (section 4.4). Our HF radar data reliably describe mesoscale flow features, such as a poleward moving jet that develops along the coast north of Pt. Reyes during relaxation periods (section 5.1) and persistent cross-shore differences in the response of currents to subtidal wind forcing (section 5.3). Analysis of high-frequency tidal, diurnal and inertial current fluctuations reveals consistent spatial patterns (section 6), and, in particular, patterns of M_2 tidal variability suggest the propagation of internal tidal waves from the shelf break (section 6.1). These results are discussed in detail in section 7, with an emphasis on their relevance for coastal biological processes.

2. Data and Methods

[8] Here we analyze the initial 8 months of HF radar surface current data from between May and December of 2001. In addition to HF radar surface currents, five WEST moorings measuring water temperature, sea surface wind velocity and subsurface currents were deployed in the area (Figure 1). Four of these moorings (C90, D90, D130, E90) are within the zone of HF radar coverage. Furthermore, an extensive oceanographic cruise was conducted in the Bodega-Reyes region from 17 May to 15 June 2001, during which time 19 surface drifters were released and tracked. Wind data are available from the National Data Buoy Center (NDBC) meteorological buoy number 46013, which is located near the center of the radar coverage area. The

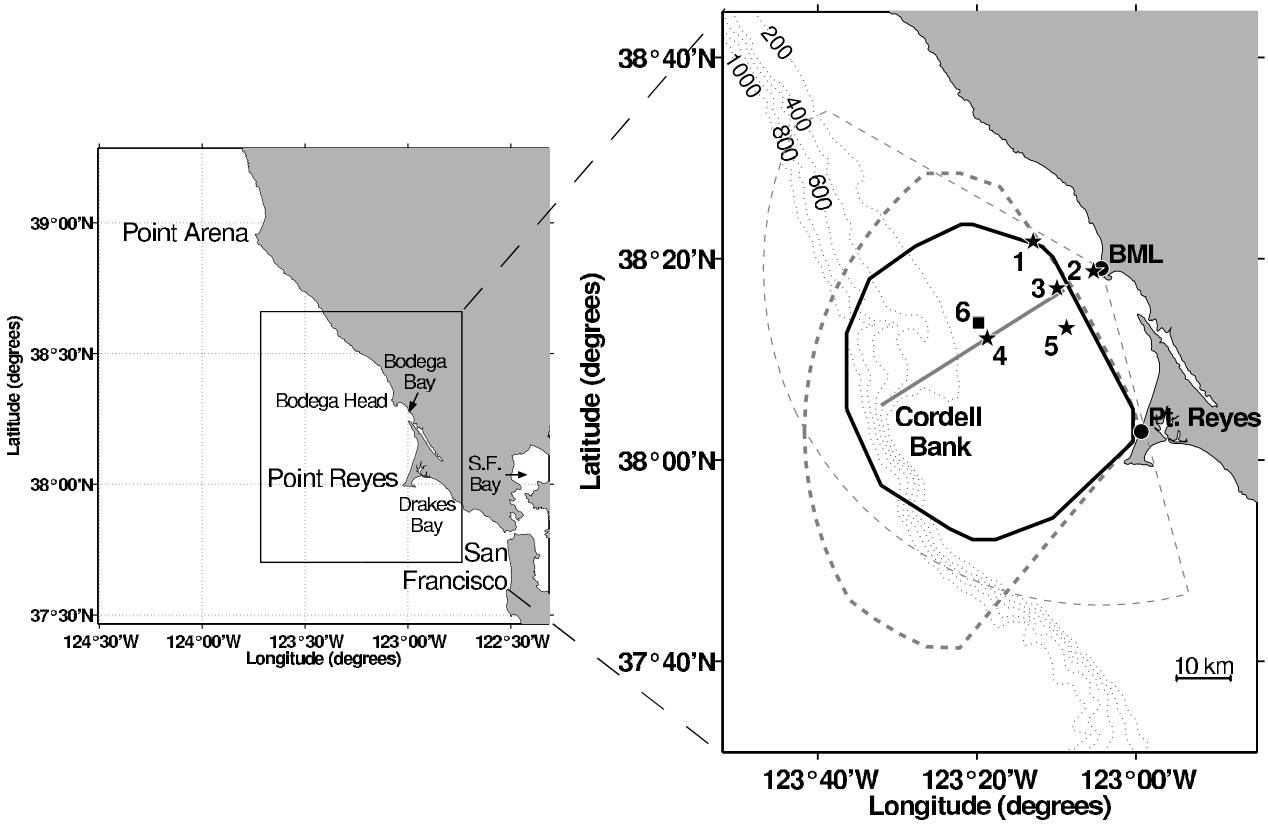

Figure 1. (left) General area of study and (right) HF radar coverage areas. On radar coverage areas map, thin and bold dashed shaded lines indicate coverage areas by radial current vectors from radar stations located at Bodega Marine Lab (BML) and Point Reyes, respectively. The coverage area of total current vectors is outlined by the solid black line. The solid shaded line in the center of the panel indicates the position of the D-line cross-shore slice of current data. Five-point stars show the locations of the five WEST moorings, and the black square gives the location of the NDBC buoy. Numbering is as follows: (1) E90 mooring; (2) D40; (3) D90; (4) D130; (5) C90; and (6) NDBC 46013 buoy. Note that the coverage area of total current vectors is less than the area of overlap of the two radial coverages due to minimum requirements for data acceptance (minimum of three radial currents, grid point must have data 40% of the time, etc.).

CODAR, mooring, and drifter data were collected as a part of the WEST study (http://www-ccs.ucsd.edu/coop/west).

2.1. HF Radar Data

[9] HF radar stations measure ocean surface currents by calculating the Doppler shift of returning energy that is Bragg scattered off "short" surface gravity waves [*Paduan and Graber*, 1997]. The difference between expected and observed Doppler shift is used to calculate the component of the total surface current moving toward or away from the radar station. Two or more "radial current" speeds from spatially separated radar locations are combined by a least squares method to calculate a total surface current vector [*Lipa and Barrick*, 1983; *Barrick and Lipa*, 1986]. The vertical depth of flow in the water column that is felt by the radar signal based on Bragg scatter is on the order of 1 m for the 12.5 MHz units used in this study [*Stewart and Joy*, 1974; *Barrick et al.*, 1974]. Extensive reviews of the basic functioning and operation of HF radars can be found in *Prandle* [1991] and *Paduan and Rosenfeld* [1996].

[10] Two CODAR radar antennas were installed in May 2001, at the Bodega Marine Lab (BML), located on Bodega Head, and along Point Reyes Peninsula (Figure 1). The antennas operate at a central frequency near 12.5 MHz, with a maximum horizontal range of 50–70 km. Radial current maps are obtained every 15 minutes and then averaged to produce hourly maps of radial currents, along with a measure of high-frequency variability in the radial current. In order to calculate the "total surface current" (i.e., vector velocities), radial maps from the two radar stations are combined in the area of signal overlap (Figure 1). In 2001, the radar coverage area from our array comprised approximately 2200 km^2 and ranged in latitude from 37.85°N to 38.40°N. Total currents on a 2 km by 2 km grid were calculated by combining all radial currents less than 1.0 m/s and originating within 2 km of a grid point.

[11] We required a minimum of 3 radial vectors, with at least one from each radar site, for the calculation of a total current. Total currents were rejected if they were greater than 1.0 m/s or they had a geometric dilution of precision (GDOP) [*Wells and Beck*, 1987; *Chapman and Graber*, 1997] greater than 2. We also used a second estimation of the error in a total current that is similar to the mapping error but takes into account the measured variability in the

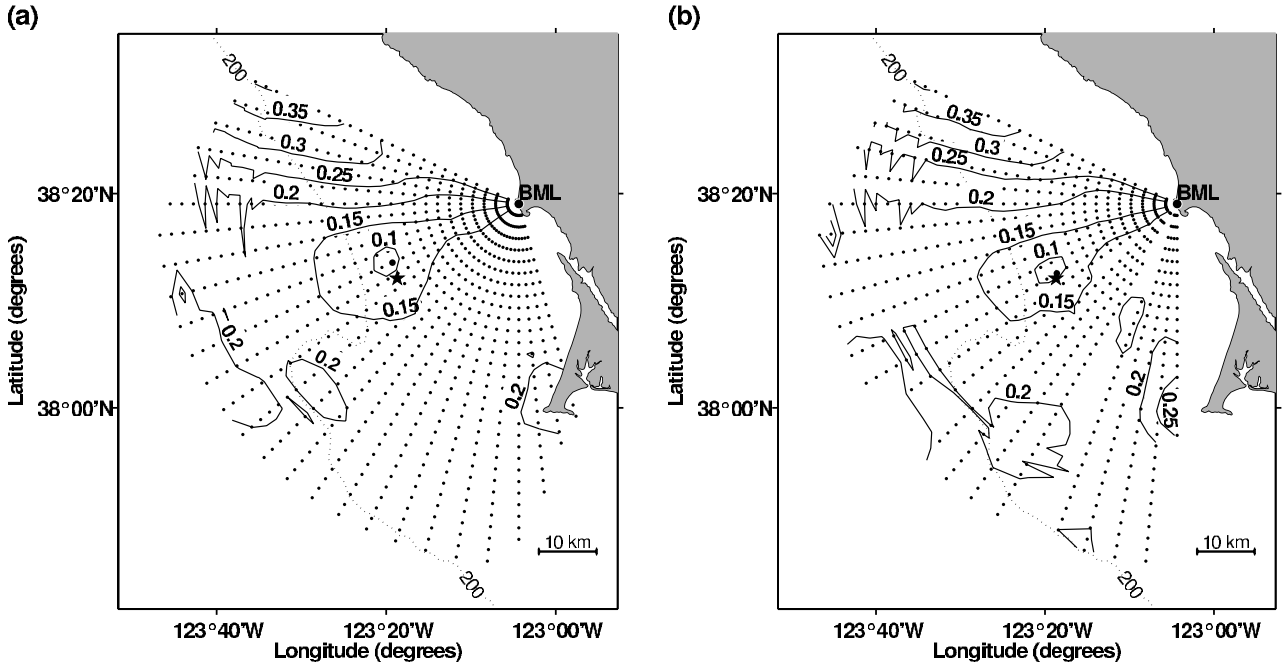

Figure 2. Root-mean-square (RMS) differences in m/s between radial HF radar currents from the BML radar station and the radial component of 5 m ADCP data from the D130 mooring. In Figure 2a, radial HF radar currents were calculated using ideal radar patterns, while in Figure 2b, measured radar patterns were used. A fire-point star indicates the mooring location, and the grip point of minimum RMS difference is indicated by a large black dot. Note the absence of a significant number of grid points from Figure 2b due to the low number of current vectors at those points using measured radial patterns.

radial currents [*Lipa*, 2003]. If this error vector was greater than 0.18 m/s in magnitude then the current estimate for that grid point and time period was omitted. Given that our CODAR radial currents have a noise level of order 0.06–0.10 m/s (see discussion of measured vs. ideal radar patterns below), this criterion imposes roughly a two to three standard deviations cutoff, and serves well in balancing data quality for a single grid point against data coverage over the domain. Finally, in analyses of the time-dependent surface current field, grid points were only included if valid total current vectors were available more than 40% of the time.

[12] The resultant spatial pattern and extent of radar coverage is shown in Figure 1. The radar coverage area off Pt. Reyes and Bodega Bay extends beyond the shelf break and encompasses Cordell Bank, a major offshore pinnacle. Data availability was high over the majority of the area, with 77% of the grid points having valid data more than 70% of the time. Coverage in the area directly between the two radar stations was poor because of the colinearity of radial current vectors, as well as partial blocking of the BML radar signal.

[13] The proximity of nearby land or metallic objects within a wavelength of the antenna distorts its classic ideal pattern. If uncorrected, this distortion produces a bearing angle error in the placement of radial current vectors [*Barrick and Lipa*, 1999]. While field measurements of radar patterns can be used to correct for the placement error due to signal distortion, only a few tests of these "measured" radial currents have been conducted [*Paduan et al.*, 2001; *Kohut and Glenn*, 2003; *Paduan et al.*, 2005]. Further, the corrected data results in undesirable spatial discontinuities in radial current vector coverage requiring angular interpolation to achieve adequate data coverage. In our data, only minor deviations from an ideal radar pattern were evident in the radar pattern emitted by the station on Point Reyes Peninsula, while that of Bodega Marine Lab was significantly different from the ideal pattern. Correcting for the distortion of the signal from Bodega resulted in significant spatial gaps in radial current coverage without angular interpolation (note absence of grid points in Figure 2b). The number of grid points with >40% coverage decreased by 15%, while grid points with >60% coverage decreased by 24%. This decrease was largely due to the concentration of radial currents in certain angular bins. The decrease in percent coverage does not necessarily indicate lower-quality data, but could indicate that distortion of the radar pattern lead to real gaps in angular coverage by radial currents.

[14] To assess any quality improvements obtained through using the measured BML radial pattern, we compared radial currents from measured and ideal radar patterns by calculating cross correlations and RMS differences between radar data and 5 m moored ADCP data. Radial ADCP data was computed by taking the component of the total ADCP current that lay along the line from the grid point to the radar station. Minimum RMS differences for both ideal and measured radar patterns were on the order of 0.06 to 0.10 m/s (Table 1). Though some of this difference is undoubtedly due to intrinsic noise in radar measurements, a significant portion of this difference might be attributable to real vertical shear in the horizontal velocity (J. T. Kohut

Table 1. Root-Mean-Square Differences Between HF Radar Radial Currents From Bodega Radar Antenna and the Radial Component of 5 m Acoustic Doppler Current Profiler (ADCP) Data[a]

	Ideal Radar Patterns		Measured Radar Patterns	
Mooring	Distance to Minimum RMS, km	Minimum RMS Difference, m/s	Distance to Minimum RMS, km	Minimum RMS Difference, m/s
C090	0.69	0.074	0.69	0.062
D090	1.85	0.062	1.08	0.061
D130	2.84	0.090	0.88	0.082
E090	3.93	0.075	2.93	0.076

[a]Data used in comparisons dates from 7 June 2001 to 17 October 2001 because measured radial patterns were not available before June 2001, and there was a significant data gap in late October 2001.

et al., Characterizing observed environmental variability with HF Doppler radar surface current mappers and acoustic Doppler current profilers, submitted to *IEEE Journal of Oceanic Engineering*, 2005, hereinafter referred to as Kohut et al., submitted manuscript, 2005). Minimum RMS differences and the distance from the WEST mooring to the HF radar grid point where the minimum occurred consistently decreased when measured radar patterns were used. Nevertheless, improvements were slight (0–16% decrease in minimum RMS difference). At D130, there was a small improvement in the location of the area with the highest agreement by 2 km (Figure 2). We elected to use the uncorrected radial data (ideal radar patterns) in this analysis, as the improvement in using corrected radial data does not merit the loss of continuity and extent of spatial coverage. Nonetheless, improvements in data agreement indicate that measured radar patterns should be used in the future if problems with spatial coverage can be solved through angular interpolation of radial currents.

2.2. Mooring Data

[15] Five moorings were deployed off Bodega Bay from April 2001 to April 2003 as part of the WEST project (Figure 1). Four of these moorings (D90, E90, C90, and D130) were within the region of HF radar coverage. Of interest are the data on subsurface current velocity. Currents were measured with buoy-mounted, downward looking 300 kHz ADCPs (acoustic Doppler current profilers), manufactured by RD Instruments (http://rdinstruments.com). Data were obtained every minute and had a vertical resolution of 2 m. The uppermost bin is centered at 5 m below the surface (6 m depth on D90 mooring). These data were hourly averaged and compared with HF radar data.

2.3. Wind Data

[16] Hourly wind data are available from NDBC (National Data Buoy Center) buoy 46013, deployed at 38.23°N, 123.33°W, 25 km west of Bodega Bay (Figure 1; http://ndbc.noaa.gov). The wind stress vector, given by $\vec{\tau} = \rho C_D |w| \vec{w}$, was calculated from the hourly wind data with the Air-Sea Matlab toolbox (http://woodshole.er.usgs.gov/operations/sea-mat). Wind velocity was corrected from 5 m recorded height to 10 m standard height and the coefficient of drag used was from *Large and Pond* [1981].

2.4. Drifter Data

[17] Nineteen drifters were deployed off Bodega Bay between 20 May and 13 June 2001. Drifters were a variation on the WOCE "holey sock" drifter, with the 6 m drogue centered at 7.5 m depth (i.e., drogue was between 4.5 and 10.5 m). Positions were obtained from GPS and recorded every 20 minutes. Lagrangian velocity was calculated from a central difference of two positions. Anomalously large velocities (>1.0 m/s) or changes in velocity ($>6 \times 10^{-5}$ m/s^2), which appeared as spikes in the time series, were removed from the data. Of the 19 drifters released, several did not cross the radar coverage region, while others crossed more than once. This produced a total of 19 partial drifter tracks that are entirely inside the radar coverage area. These 19 partial tracks varied in duration from 2 hours to 6 days. Pseudo-eulerian drifter velocities and the actual drifter tracks were compared with HF radar surface currents and virtual particle tracks, respectively.

[18] Virtual particle tracks derived from HF radar currents were calculated using a second-order method with a variable time step [*Bennett and Clites*, 1987]. The size of the time step was adjusted so that no particle moved more than 0.25 km (an eighth of the grid spacing) in a single time step. The maximum time step size was one hour. Particle tracks ("pseudo drifters") were calculated to match up with the 19 observed drifter tracks, i.e., pseudo drifters were started at the same place and time as the real drifters. The second-order method produced particle tracks very similar to a first-order algorithm with a fixed 1 hour time step, suggesting that little improvement would be obtained by using a higher-order algorithm.

2.5. Data Analysis

[19] Hourly data sets were obtained for all data sets over the period of interest: May–December 2001. Data gaps were filled as needed, using the average of linear-spatial and linear-temporal interpolation. For HF radar data, this interpolation was only performed on grid cells with 60% or greater coverage over the entire data set. Temporal data sets, such as the ADCP data, were filled using linear-temporal interpolation alone. Subtidal records of currents and winds were obtained by applying the 38 hour PL64 low-pass filter [*Beardsley et al.*, 1985] to remove all tidal, diurnal and inertial fluctuations (the inertial period is 19.4 hours at this latitude). When current vectors are decomposed into alongshore and cross shore, the alongshore orientation is taken as 330° (i.e., 30° west of north), which is roughly parallel to the coast and to isobaths away from Cordell Bank. In other analyses, currents at a specific location are decomposed into flow variability along a principle axis and an orthogonal minor axis.

[20] In comparing radar and ADCP velocity data, interpolated HF radar surface currents were compared with the uppermost bin (5 m depth) of ADCP data from the WEST moorings. Cross correlations were calculated on the along-

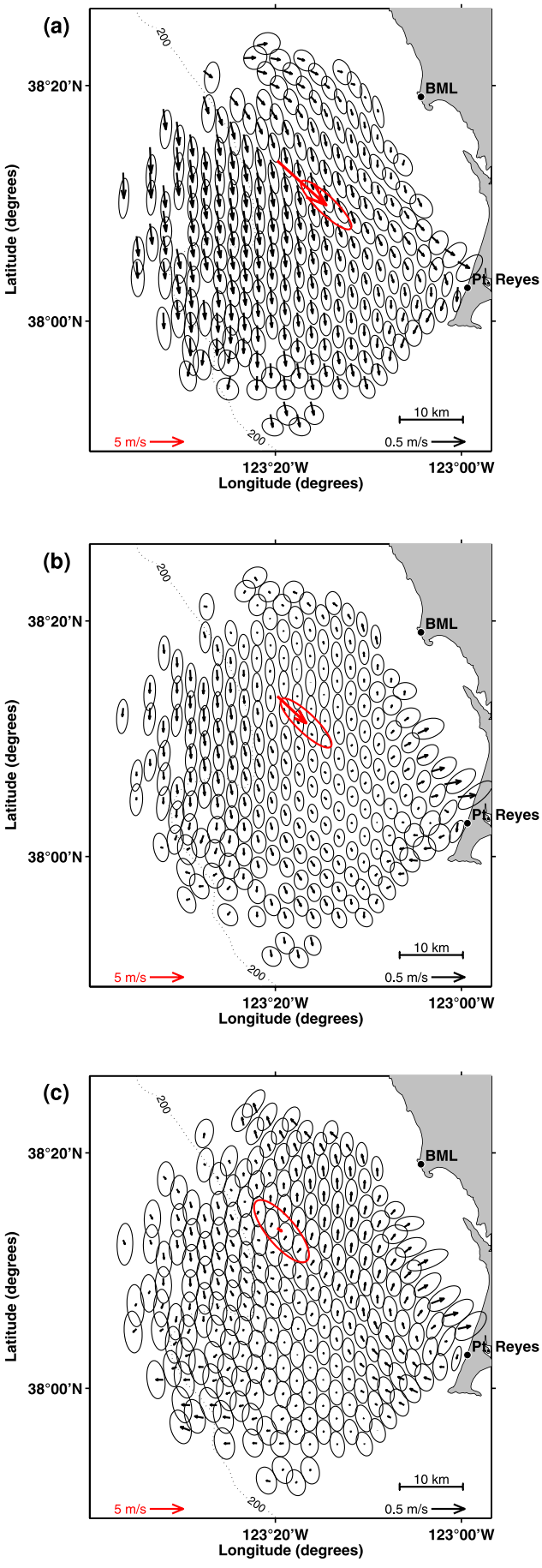

shore and cross-shore components of the currents, as well as on the complex current, $u + iv$. Critical values for the magnitude of complex correlations are calculated assuming perfect covariance between the alongshore and cross-shore components of the currents. In this case, the critical value reduces to that of a real-valued correlation with the same number of observations. This is more conservative than assuming imperfect covariance between the two components. We use a nonreplacement bootstrap to calculate 95% confidence limits on the phase of the complex correlation. An alternative measure of the correlation between vector-valued quantities described by *Crosby et al.* [1993] was also calculated. We also calculated root-mean-square (RMS) velocity differences between HF radar and ADCP data.

[21] Tidal analysis by the least squares method was performed on the complex-valued current using the uninterpolated HF radar data set with the T_tide Matlab toolbox [*Pawlowicz et al.*, 2002]. Eight months of data were included in the analysis (May–December 2001). Only those grid points that contained at least 70% valid data were included. Nodal corrections were included in the determination of the tidal harmonics. Confidence intervals in the tidal parameters were calculated based on an uncorrelated bivariate colored noise model. Only harmonics with signal-to-noise ratio greater than 2 were included in the final predicted tides. An identical tidal analysis was performed on the moored ADCP data from 5 m and 9 m, and on the NDBC 46013 wind data.

[22] Other analyses included autocorrelation, power spectra, rotary spectra [*Gonella*, 1972], cross correlation, cross spectra, signal demodulation and EOF (empirical orthogonal function) analysis. For the spectral analysis, estimates of the power spectral density of the complex-valued current, as well as the alongshore and cross-shore components, were computed using the multitaper method described by *Percival and Walden* [1993]. In this method the power spectral density is estimated using a nonlinear adaptive method [*Thomson*, 1982] that combines modified periodograms from various segments of data. Segments 24 days in length were used. For cross spectra, the square coherence of the cross-spectral density between colocated radar and 5 m ADCP data was calculated using the same data sets used for estimation of the power spectral density [*Shumway and Stoffer*, 2000]. In this case, periodograms were calculated over eight day segments of data before being averaged to produce final coherence. This produced lower-frequency resolution than that for the power spectra, but increased certainty in measured values. Cross spectra were also obtained for the relationship between radar data of surface currents and wind data from the NDBC buoy. Empirical Orthogonal Functions (EOF) were calculated using subtidal data from 1 June 2001 to 1 September 2001 considering

Figure 3. Mean surface currents for the months of (a) June, (b) July, and (c) November 2001. Vectors indicate mean current at that grid point, while ellipses indicate standard deviation of currents along and perpendicular to principal axis of current variability. Red arrows and ellipses give mean wind velocity and standard deviation at the NDBC 46013 buoy. Note that only half the HF radar grid points are shown to improve visual clarity.

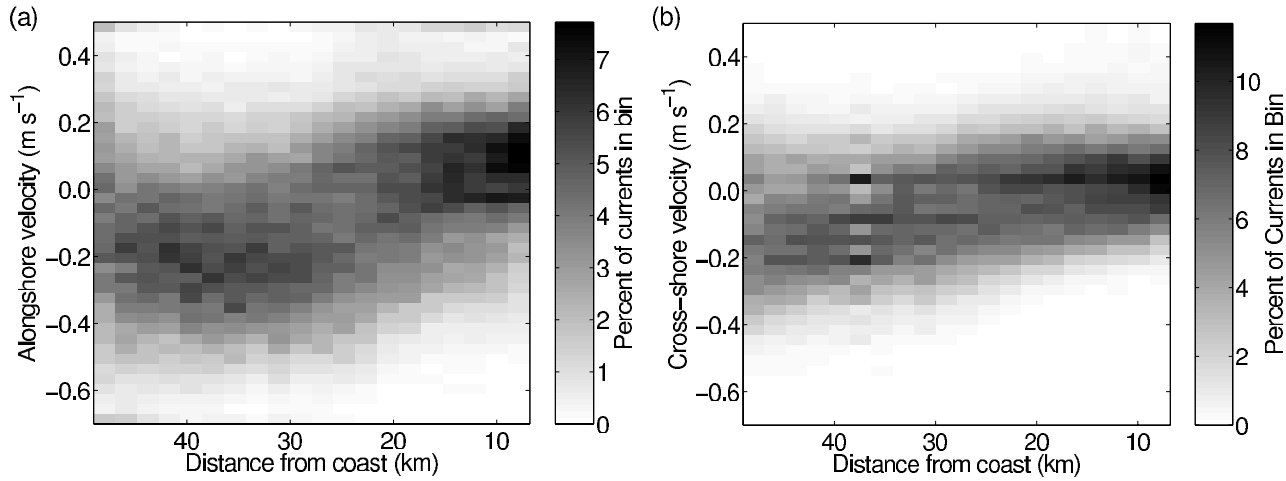

Figure 4. Distribution of (a) alongshore and (b) cross-shore currents as a function of distance to the coast along the D-line of WEST moorings from May to December 2001. Dark shading indicates that a significant percentage of the currents at that distance from the coast were of that magnitude. Note that nearshore is to the right of each panel.

both components of the current vectors as independent variables following *Preisendorfer and Mobley* [1988].

3. General Description of Surface Circulation

3.1. Monthly Mean Surface Flow

[23] Southward (equatorward) flow dominates the Bodega-Reyes region during the months of the upwelling season, with mean flows up to 0.25 m/s in June 2001 (Figure 3a). Over the inner shelf, mean flow was near-zero, while strongest southward flows were observed over the slope and seaward of the slope. Close to Pt. Reyes there is a westward deflection and strengthening of the mean southward flow, and at the northern end of the radar domain currents are more eastward, associated with the more SE-NW orientation of the coastline north of the data region. While the radar data provides a coherent pattern of mean flow, there is significant variability with standard deviations of the order of the mean (or quite a bit larger over the inner shelf where the mean is near-zero). This variability is primarily aligned with the mean flow. Circular ellipses were also observed in the extreme north and south of the radar domain, suggesting that flow variability is not polarized in the alongshore direction. This lack of polarization is most likely indicative of increased methodological noise along the margins of our domain. Monthly mean flow in May 2001 was similar to June, but had somewhat smaller mean velocities. These patterns of flow are consistent with strong mean winds oriented toward the equator during this time period.

[24] In contrast to the southward mean flow in June, monthly means in July 2001 exhibit weak northward flows over the inner shelf, near-zero mean flow over the mid/outer shelf, and weaker southward means over the slope (Figure 3b). This is consistent with weaker mean wind forcing in July. While this weaker southward flow may be observed over the shelf during any month of the upwelling season, following *Largier et al.* [1993], this is characteristic of later summer, with the weakening of wind forcing during the transition from the upwelling season (April–July) to the relaxation season (August–November). The radar data provides more spatial pattern to the earlier analyses of mooring data [*Winant et al.*, 1987; *Largier et al.*, 1993], showing mean offshore flow at Pt. Reyes and mean onshore flow immediately north of the point, reflecting the strength of a clockwise eddy that sets up in this vicinity during northward flow past the point. Further north, off Bodega, the poleward mean and associated variability are aligned alongshore – consistent with earlier results from moorings during CODE and NCCCS [*Kosro*, 1987; *Largier et al.*, 1993]. Monthly mean surface circulation in August 2001 is similar to that of June 2001, while September and October show poleward flow along the coast similar to July.

[25] Although poleward flow over the shelf is strongest during fall and early winter, mean currents generally remain poleward throughout the winter in spite of the persistence of weak southward wind forcing in this region [*Largier et al.*, 1993; *Dorman and Winant*, 1995]. This poleward mean flow can be seen in the surface circulation observed in November 2001 (Figure 3c). Significant and well-organized poleward mean flow is evident over the shelf (up to 0.15 m/s), with near-zero mean and large standard deviations observed over the slope. The region of clockwise (anticyclonic) mean vorticity is again evident immediately north of Pt. Reyes. Monthly mean surface flows in December and January 2001 are similar to November, though current variability increases during these two months.

3.2. Cross-Shore Structure of Surface Current Distributions

[26] Further insight on typical currents is obtained from examining the distribution of current velocities at different distances offshore of BML, along the D-line axis of moorings and hydrographic surveys (Figure 1). Distributions of both alongshore and cross-shore velocities are shown in Figure 4. Again, stronger equatorward flows over the outer shelf and slope are evident, but there is a

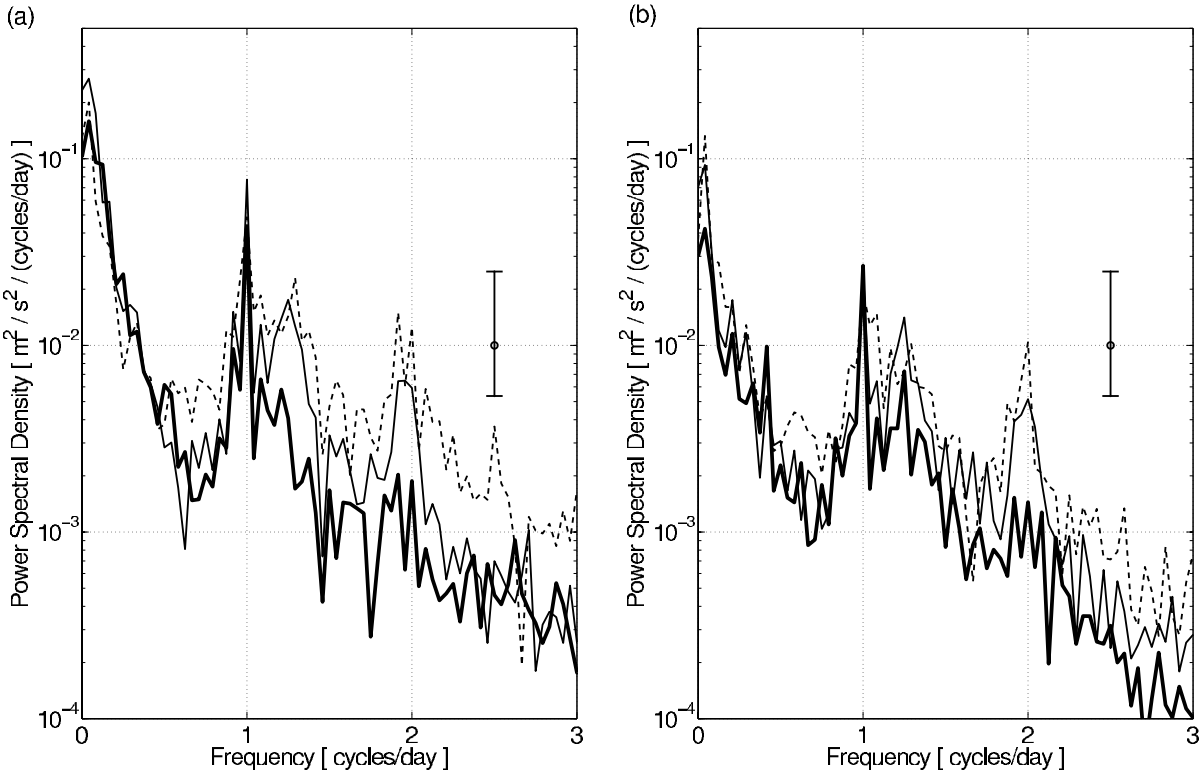

Figure 5. (a) Alongshore and (b) cross-shore power spectral densities of HF radar data for three different locations along the D-line of WEST moorings. The bold line shows spectra from a radar grid point 8 km from shore (where the water column is 90 m deep), the thin solid line is 23 km from shore (120 m depth), and the dashed line is 38 km from shore (240 m depth).

maximum found between 30 and 40 km offshore, where currents up to 0.5 m/s are observed (Figure 4a). In this region, equatorward currents between 0.2 and 0.3 m/s are most common and poleward currents are rare, although slack currents are observed at times. Over the shelf, the distribution of alongshore current becomes progressively less equatorward, with poleward currents more probable over the inner shelf. Inshore of 15 km, poleward surface

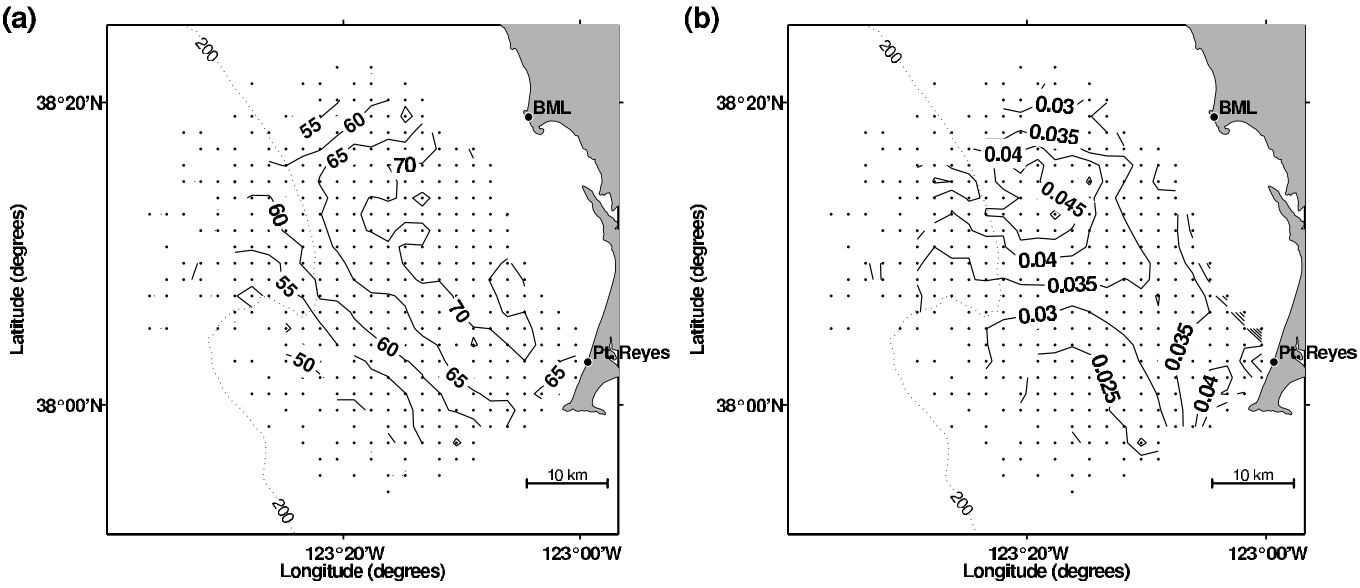

Figure 6. Percent of (a) overall variance and (b) actual variance contained in subtidal fluctuations. Actual variance is in units of m^2/s^2. Subtidal currents were calculated by applying the PL64 filter to the interpolated HF radar data set.

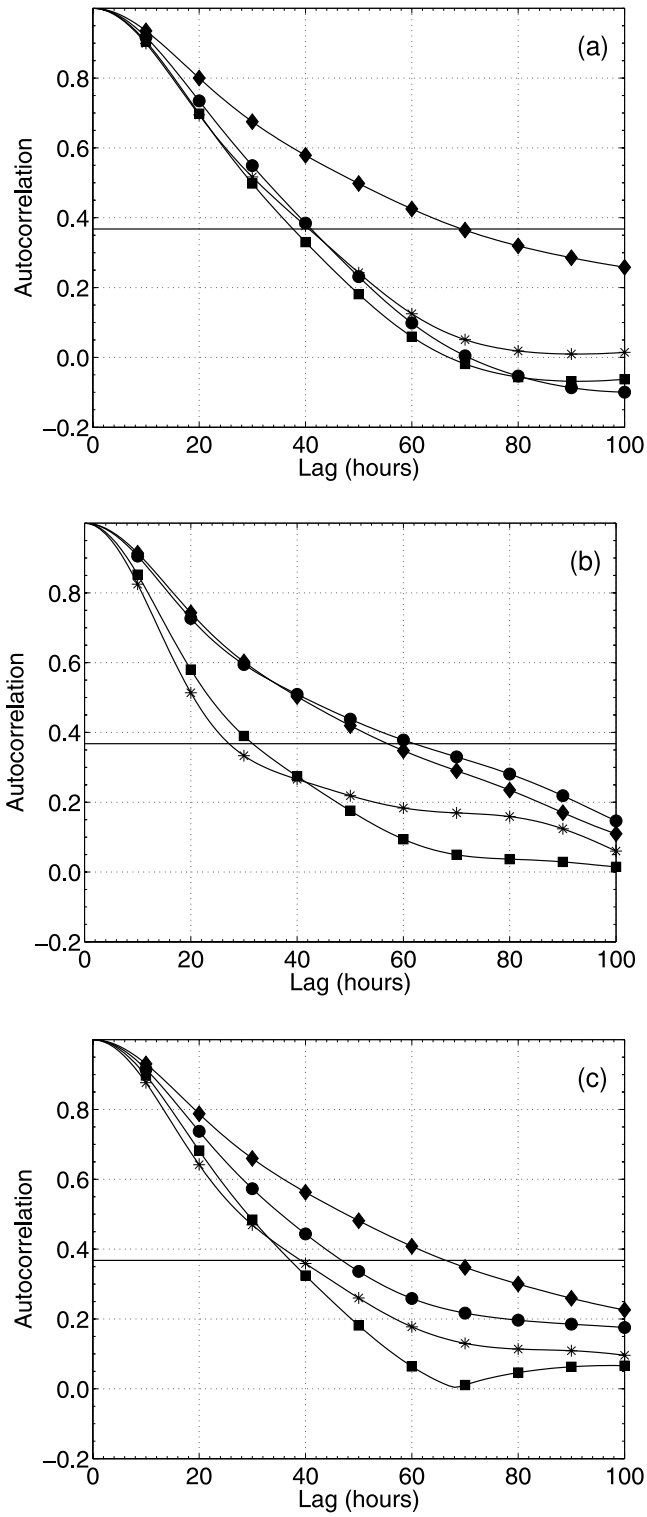

Figure 7. Autocorrelations of subtidal HF radar surface currents for (a) alongshore, (b) cross-shore, and (c) complex currents from grid points nearest WEST moorings. Line with filled circles is for the grid point nearest C90, squares is D90, diamonds is D130, and stars is E90. Horizontal line is the *e*-folding scale (e^{-1}) used to determine temporal autocorrelation scale.

currents of order 0.15 m/s are most common and poleward velocities can exceed 0.2 m/s. A similar, though considerably weaker, pattern is evident in the distribution of cross-shore currents, with offshore flow increasing with distance from the shore (Figure 4b). Nonetheless, this pattern is understood to reflect the structure of the alongshore flow due to an imperfect choice of alongshore orientation, as well as the lack of depth integration; current velocities of order 0.1–0.2 m/s do not represent Ekman transport. However, the general trend to stronger offshore flow at greater distances from the coast points to a general veering of currents over the outer shelf and slope toward a more westward (more offshore) orientation.

3.3. Temporal Variability

[27] Spectra of the temporal variability in surface currents are shown in Figure 5 for three radar grid points along the D-line of WEST moorings. There is a common red spectral pattern, with peaks in variance at semidiurnal, inertial, and diurnal frequencies, and a well-defined increase in spectral energy in the subtidal frequency band characteristic of synoptic fluctuations in wind forcing (0.1–0.5 cpd). Spectral energy is noticeably higher in alongshore currents (Figure 5a) than cross-shore currents (Figure 5b), consistent with the stronger alongshore flows previously noted. There is a trend toward lower power levels at subtidal, inertial and semidiurnal frequencies at the grid point closest to shore, though the diurnal peak is highest nearshore. This last pattern is consistent with forcing by the diurnal sea breeze, though the increase in energy nearshore is relatively modest.

[28] In subsequent analyses, we give attention to the tidal band in section 6 (including semidiurnal, inertial, and diurnal variability) and the wind band in section 5 (subtidal variability associated with synoptic meteorological forcing). Subtidal variability in surface currents is dominant, accounting for 45–75% of the overall variance in the HF radar data set (Figure 6a). Strongest subtidal variability is observed in the vicinity of Pt. Reyes and over the outer shelf off Bodega Head, in the vicinity of D130 (Figure 6b). Differences between patterns of overall subtidal variance and percent variance in the subtidal band are due to a marked decrease in tidal variance in shallower waters and an increase in tidal variance in the vicinity of Cordell Bank (see section 6).

[29] The dominant timescale of subtidal variability can be obtained from autocorrelation plots (Figure 7). Over the inner and midshelf, correlation scales for alongshore flow were on the order of 40 hours, while a scale of order 80 hours was obtained for locations over the outer shelf and slope (D130 mooring; Figure 7a). Cross-shore currents exhibit shorter timescales and much more spatial pattern, with a scale of about 30 hours at E90 and D90, and 60 hours at C90, comparable with that over the outer shelf at D130 (Figure 7b). Estimates of the correlation scale from complex autocorrelations combine cross-shore and alongshore variability (Figure 7c). The spatial pattern of this complex correlation scale (Figure 8) shows longer timescales for currents over the outer shelf off Bodega, with shorter timescale variability both nearshore and in the south, off Pt. Reyes. Autocorrelation analyses on data that included tidal band variability yielded significant reductions in the timescale of cross-shore and alongshore current autocorrelations, indicating that tidal band variability is important.

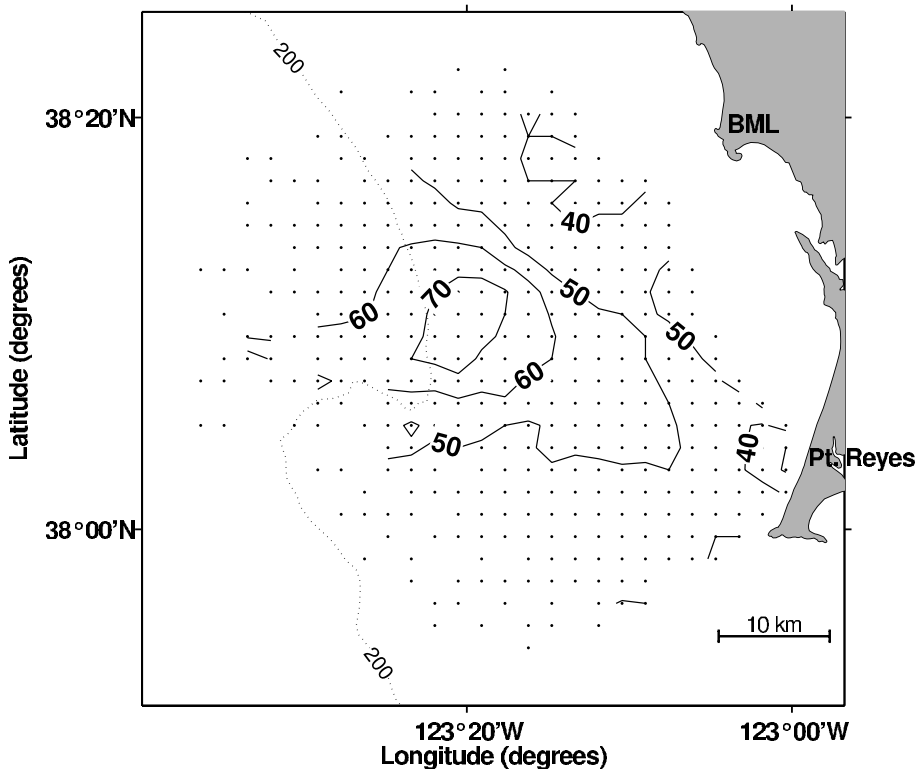

Figure 8. Spatial pattern of temporal autocorrelation scales of complex currents for subtidal HF radar data. Autocorrelation scale is calculated for each grid point based on the *e*-folding scale (Figure 7).

[30] The spatial uniformity of this temporal variability is examined by calculating correlation coefficients between current velocity at one specific grid point (e.g., near the D130 mooring) and velocities at all other grid points in the radar domain. All frequency bands are included in this analysis. Spatial patterns of complex correlation coefficients and complex phases were very similar to those found for comparisons between radar data and near-surface ADCP data discussed in detail below (section 4.2; Figures 11a and 11b). Temporal variability was coherent over all of the radar domain, with correlation coefficients above 0.5 over the majority of the grid points. Correlation coefficients decreased with distance from the grid point used in the comparison and the region of highest values was elongated in the alongshore direction. The complex phase, a measure of the orientation of variability in one current velocity time series with respect to another, was between $-10°$ and $10°$ in all of the radar domain except the northern and southern boundary, indicating that variability in flow direction was also relatively homogeneous over space.

4. Comparison of Radar Data With Acoustic Doppler Current Profiler (ADCP), Wind, and Drifter Data

4.1. Spectral Comparisons Between Radar, ADCP, and Wind Data

[31] Rotary spectra for HF radar surface currents near the C90 mooring are shown in Figure 9a, alongside spectra for C90 ADCP near-surface currents from bins centered at 5 m and 9 m depth (Figures 9b and 9c), and the spectrum for winds at the NDBC buoy (Figure 9d). The spectra of currents are qualitatively similar, with the red nature of the spectrum, the energetic wind band, and the peaks at diurnal, inertial and semidiurnal frequencies being common to both radar and ADCP spectra. Subtidal and semidiurnal spectral levels are similar for radar and ADCP data. Further, the clockwise nature of the inertial-diurnal peaks and the nonpolarized semidiurnal peak are evident for both types of data. Wind spectra are dominated by low-frequency and diurnal variability (including what is presumably a diurnal harmonic at the semidiurnal frequency), with notable clockwise polarization of the diurnal peak. However, there are two notable differences between the surface radar spectrum and the near-surface ADCP spectra.

[32] 1. The large diurnal peak in radar data is evident in the wind spectrum and also in the 5 m ADCP data, but it is much weaker at 9 m depth. Further, the clockwise dominance of the diurnal peak is weaker in ADCP data, owing to enhanced anticlockwise diurnal variability at both 5 and 9 m. These differences between 0, 5 and 9 m are likely to be a real near-surface shear associated with diurnal wind forcing of the surface.

[33] 2. The clockwise dominance evident in the inertial peak in radar data is more dramatic and encompasses a wider range of frequencies in the ADCP spectra, extending from inertial to supertidal frequencies. In comparing the surface and 5 m spectra, it is evident that this enhanced polarization results from a combination of a decrease in anticlockwise variability and an increase in clockwise variability (e.g., compare Figures 9a and 9b at frequencies between 1.5 and 2 cpd).

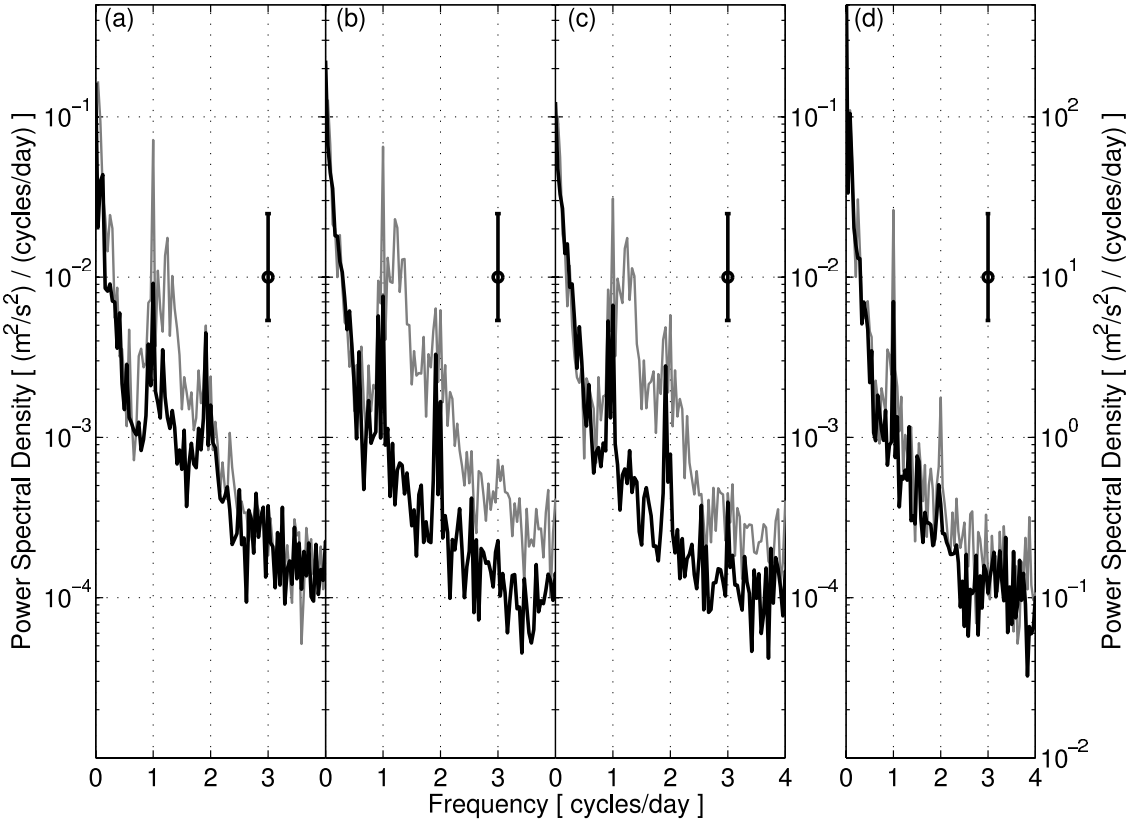

Figure 9. Power spectral densities from HF radar, ADCP, and wind data. The (a) HF radar spectrum was calculated using the grid point nearest the C090 mooring. (b, c) Spectra are from 5 m and 9 m ADCP data at the C090 mooring, respectively. (d) Spectrum for NDBC 46013 wind data. The shaded line shows the power in clockwise-rotating fluctuations, while the black line indicates the power in counterclockwise-rotating fluctuations. Error bar indicates 95% confidence interval.

[34] Spectra of currents from other mooring locations have a similar structure with subtidal, diurnal, inertial and semidiurnal peaks evident at each. A more detailed analysis of spatial patterns of each of the dominant peaks is given in sections 5 (subtidal fluctuations) and 6 (tidal, inertial and diurnal fluctuations).

[35] Cross spectra of radar and ADCP data provide insight into covariability in currents observed at the surface and 5 m depth (Figure 10). Coherence between radar and ADCP records is strong in the wind band (<0.3 cpd) and throughout most of the tidal band (0.8 to 2.3 cpd). There is a noticeable dip in coherence between the subtidal and diurnal/inertial peaks (0.4 to 0.8 cpd), as well as between the inertial/diurnal peak and the semidiurnal peaks (1.5 to 1.8 cpd). Coherence is absent in the low-energy, high-frequency spectral band (>2.4 cpd). For all WEST moorings, semidiurnal coherence is lower ($\sim$0.6–0.7) than at diurnal or inertial frequencies ($\sim$0.8–0.95) for clockwise fluctuations, though the opposite is true for counterclockwise fluctuations. At diurnal-inertial frequencies, coherence is strongest for clockwise-rotating fluctuations, consistent with the strength of the clockwise signal (Figure 9). Significant coherence is observed between winds and radar currents at diurnal and subtidal frequencies (Figure 10b), with diurnal coherence increasing noticeably from 0.6 at D130 (not shown) to 0.7 closer to the coast (e.g., C90) where the diurnal wind forcing is stronger (C. E. Dorman et al., Buoy measured wind, wind stress and curl of the wind stress over the shelf off Bodega Bay, California, submitted to *Deep-Sea Research, Part II*, 2005, hereinafter referred to as Dorman et al., submitted manuscript, 2005). Subtidal wind-radar coherence is strongest at D130 (not shown) and C90.

4.2. Comparison Between Radar and ADCP Data

[36] We calculated cross correlations between subtidal HF radar data and near-surface ADCP data from the four WEST moorings inside the CODAR region. Correlations were performed on the alongshore and cross-shore components of the current, as well as on the complex current. An additional vector correlation described by *Crosby et al.* [1993] was also calculated. Results are summarized in Table 2.

[37] All vector and individual component correlations are significant at the 95% level for the four moorings with the exception of the cross-shore correlation at E90, which is quite low. E90 shows consistently lower correlation values, most likely because it is along the edge of the data region where HF radar data quality is somewhat lower and there is a relatively large distance between the mooring and the nearest HF radar grid point. The correlation of the alongshore component of the current is highest at D130, while vector correlations are greatest at C90, though differences are relatively small. The phase of the complex correlation

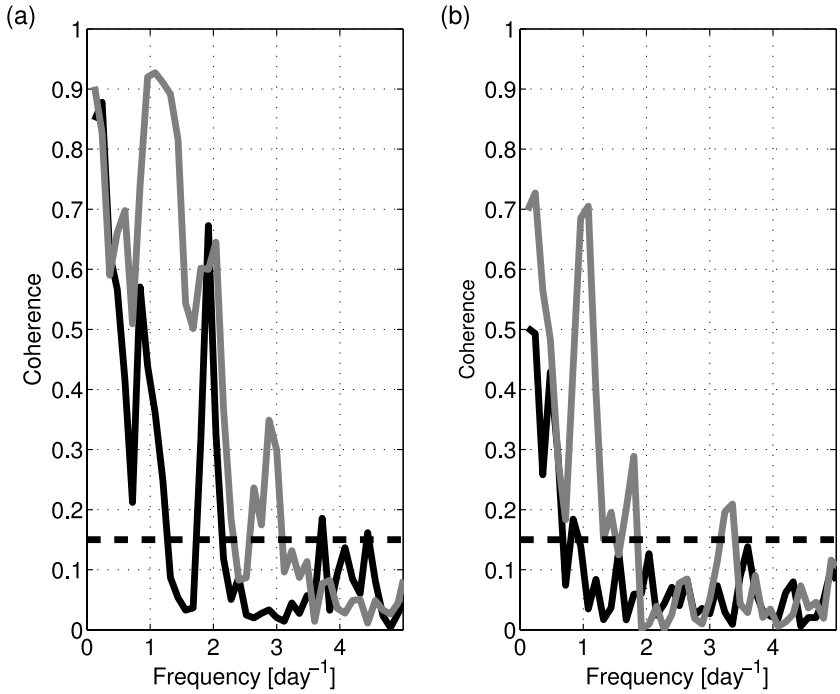

Figure 10. Coherences for HF radar data near C90 mooring with 5 m ADCP data from (a) C90 and (b) NDBC 46013 wind data. The shaded lines are for clockwise-rotating fluctuations, and the black lines are for counterclockwise fluctuations. The horizontal dashed lines give the 95% confidence interval that true coherence is different from zero for a single frequency.

indicates that subtidal ADCP currents are on average counterclockwise rotated with respect to HF radar currents by 0°–5° at all moorings except E90, where the rotation is 13° clockwise.

[38] We also calculated root-mean-square velocity differences between 5 m ADCP data and nearby HF radar data for both the unfiltered data set and subtidal data (Table 3). Data that included all frequencies show somewhat higher RMS

Table 2. Summary of Comparisons Between Subtidal HF Radar Total Current Vectors and Subtidal ADCP and Wind Measurements[a]

	Mooring				
	C090	D090	D130	E090	N13
Depth of mooring data, m	5	6	5	5	−5
Cross-shore component					
Correlation	0.92	0.85	0.83	0.04	−0.39
Critical value (95%)	0.23	0.16	0.21	0.14	0.22
Alongshore component					
Correlation	0.89	0.86	0.91	0.87	0.79
Critical value (95%)	0.19	0.17	0.24	0.18	0.25
Crosby statistic					
Correlation	0.85	0.78	0.81	0.71	0.59
Critical value (95%)	0.27	0.18	0.26	0.22	0.26
Complex correlation					
Magnitude	0.90	0.86	0.89	0.78	0.74
Critical value (95%)	0.21	0.17	0.24	0.18	0.24
Phase, degrees	−3.06	−4.19	0.79	29.08	−37.79
Lower/upper limit, degrees	−3.99/−2.14	−4.74/−3.66	0.26/1.32	27.78/30.36	−38.46/−37.09

[a]The closest HF radar grid points to each WEST mooring and the NDBC weather buoy are used in the comparisons. Data were from 8 May 2001 to 28 December 2001. Number of observations used to determine critical values is adjusted for the temporal autocorrelation scales. Critical values for the magnitude of the complex correlation are the same as that for a two-tailed, real-valued correlation with the same number of observations. Confidence intervals for the phase of complex correlations are from a nonreplacement bootstrap. Positive phase indicates that HF radar data is rotated clockwise with respect to the other data set in the comparison.

Table 3. Root-Mean-Square Velocity Differences Between 5 m ADCP Data (6 m at D090) and Nearby HF Radar Grid Points for Both Unfiltered (i.e., Including Tidal/Diurnal/Inertial Band) and Subtidal Data

	Unfiltered Data			Subtidal Data		
Mooring	Cross-Shore	Alongshore	Vector	Cross-Shore	Alongshore	Vector
C090	0.082	0.101	0.130	0.045	0.068	0.081
D090	0.073	0.121	0.141	0.050	0.085	0.098
D130	0.096	0.117	0.152	0.061	0.078	0.099
E090	0.154	0.114	0.191	0.113	0.073	0.135

differences (vector differences of 0.13–0.19 m/s) than subtidal data (0.08–0.14 m/s). Alongshore RMS differences were generally higher than cross-shore differences, consistent with stronger alongshore currents. Patterns of variation in RMS differences between moorings are similar overall to those seen in correlations. The E90 mooring had noticeably worse values than the other moorings. Nearshore moorings, with the exception of E90, had lower vector RMS differ-

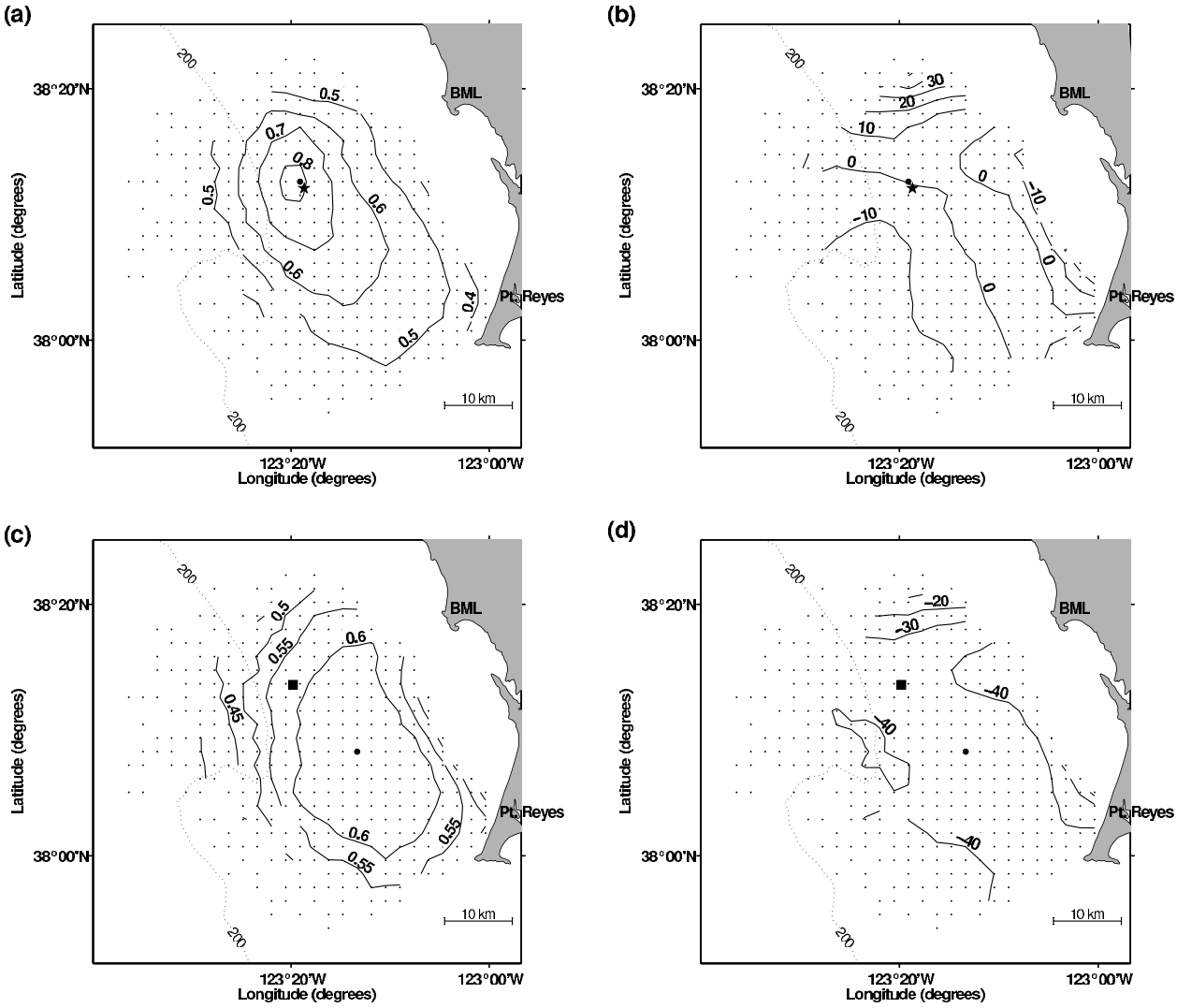

Figure 11. Cross correlations of HF radar data with 5 m ADCP data from the D130 mooring and NDBC 46013 wind stress. Data from all frequencies were used in these comparisons. (a, b) Magnitude and phase (in degrees), respectively, of complex cross correlations between radar and ADCP data. (c, d) Magnitude and phase for comparisons between radar and wind data. A positive phase indicates that ADCP or wind data are, on average, clockwise rotated with respect to HF radar data from that grid point. The location of the D130 and NDBC moorings are indicated by a five-point star and square, respectively. The grid points with the highest correlations are given by a large, black dot. A conservative estimate of the value of the magnitude of the complex correlations above which the correlation is significant at the 95% level is 0.24.

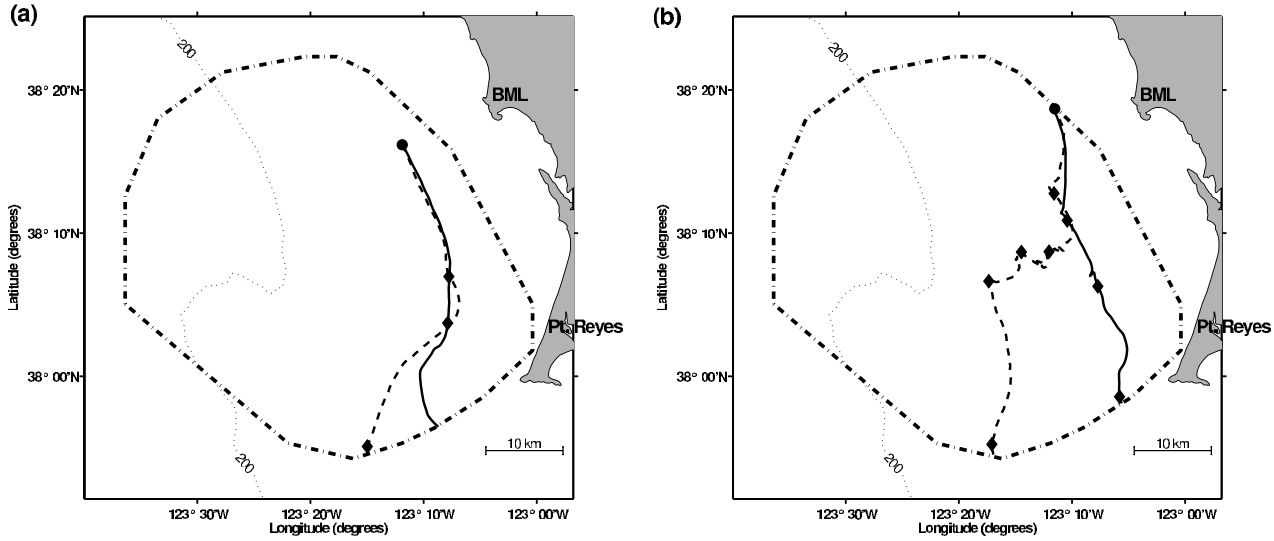

Figure 12. Comparison between real drifter tracks and HF radar–derived drifter tracks. The true path of the drifter is indicated by the dashed line, while the track derived from HF radar data that begins at the same time and place as the drifter is shown by the solid line. Shaded diamonds indicate 24 hour intervals along the tracks.

ences than the D130 moorings. Nonetheless, RMS differences of the alongshore component of the current alone were comparable at D130 and C90. These RMS differences, though significant when compared to either the mean or the standard deviation of current velocity (both of order 0.15–0.30 m/s), are consistent with those found in other HF radar–ADCP comparisons, as well as comparisons between adjacent ADCP current bins (Kohut et al., submitted manuscript, 2005).

[39] Cross correlations between near-surface ADCP data at a specific mooring and all surface radar grid points were calculated to explore the uniformity of the surface flow and to assess the directional error in radar-measured currents. Results for the D130 mooring are shown in Figures 11a and 11b. All frequency bands are included in this analysis. Complex correlations are strong in the vicinity of the mooring site (order 0.75), and phases are about 0°. Correlations are significant over the entire radar domain, but values decrease with distance, most notably in the cross-shore direction, i.e., the regions of high correlation are elongated in the alongshore direction. In all cases, there is little difference in the orientation of current variability over most of the radar domain, with the exception of the northern and southwestern edges (Figure 11b). Along the northern edge of the domain, current variability is rotated 10°–30° counterclockwise relative to D130 ADCP data, consistent with the more eastward orientation of the mean flow (Figure 3) and the coastal topography. Along the southwestern edge, currents are rotated 10°–20° clockwise relative to D130 ADCP data, consistent with the expansion of the continental shelf near Cordell Bank and the seaward deflection of currents by Pt. Reyes. A similar broad uniformity is seen in correlation maps based on ADCP data at the other mooring sites.

[40] The distance between the ADCP mooring and the location of maximum HF radar correlation is less than 3 km for all moorings, except E90 which is located on the margins of the radar domain (radar coverage between 40% and 60%). For E90, the maximum correlation is 9 km from the mooring location. The location of the maximum correlation occurred to the south of the actual mooring location for two of the moorings, to the north for one and to the west for another, suggesting that there is little consistent directional bias in the HF radar data. The phase of the location of maximum correlation was between −5° and 5° at all moorings.

4.3. Spatial Patterns of Coherence Between Radar and Wind Data

[41] The magnitude of complex correlations between wind at the NDBC buoy and radar data from all grid points are greater than 0.5 over most of the radar domain (Figure 11c). Maximum correlations in excess of 0.6 are found equatorward (downstream) of the NDBC buoy. The phases of the complex correlations indicate that HF radar variability is rotated about 30°–50° clockwise relative to winds: in the sense of Ekman veering, and in good agreement with observations of *Paduan and Rosenfeld* [1996], over the entire radar domain except the far northern edge, where phases were 10°–30° clockwise.

4.4. Comparison Between Radar and Drifter Data

[42] Radar-derived particle tracks (virtual drifters) can be compared with real drifter tracks available from May to June 2001. Although these tracks are qualitatively similar in general, particularly during persistent upwelling conditions (e.g., Figure 12a), significant differences are observed at times, particularly during transitions between upwelling and relaxation conditions (e.g., Figure 12b). In many cases, the separation between drifter and radar tracks appeared to be associated with small-scale flow structures that would not be adequately represented by radar data. However, even in

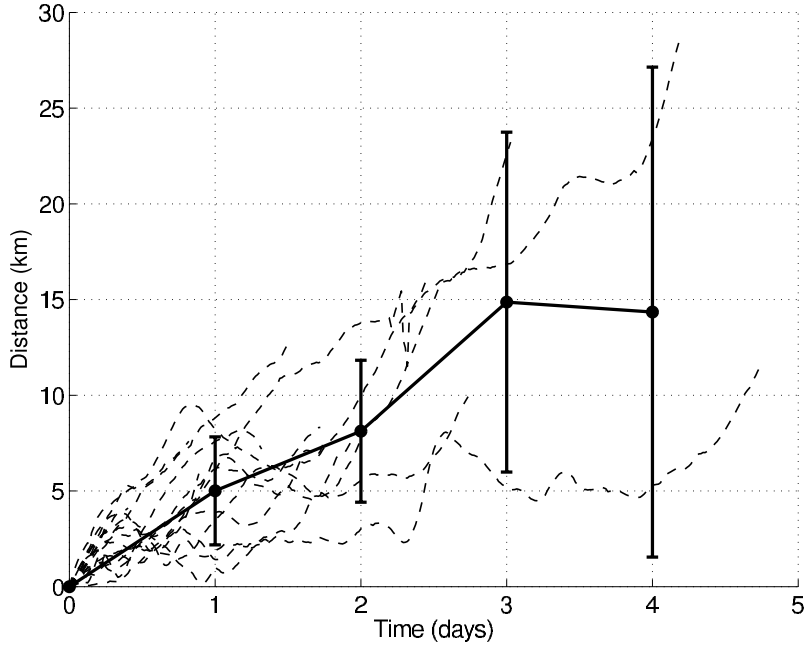

Figure 13. Separation between drifter and HF radar tracks as a function of time. Shaded, dashed lines show the separations of individual pairs of drifter and HF radar tracks. The solid line gives the mean at 24 hour intervals and the standard deviation around the mean.

the best cases there is a separation between drifter and radar-derived tracks. Plotting this separation as a function of time (Figure 13), one can see that separation rates are between 1 and 10 km/d, with an aggregated rate of 5 ± 3 km/d in this region and during this time period.

[43] The majority of the drifters were deployed during upwelling conditions (out of a total of 19 drifters, 13 moved equatorward). Of these 13 upwelling drifter tracks, 8 were seaward of the corresponding radar-derived particle track, 4 were neither seaward nor inshore of the radar track and only 1 moved inshore of the radar track. The preponderance of seaward drifter tracks is consistent with Ekman veering, in that the deeper currents experienced by the drifters are rotated clockwise relative to surface currents sampled by HF radar.

[44] Eulerian comparisons between colocated radar and drifter velocities also indicate reasonable agreement. From the 19 tracks within the radar domain, 967 velocity comparisons were obtained by pairing drifter velocities with radar velocities from within 2 km of the drifter position. Drifters typically move slower than related radar velocities (Figure 14a), with drifter velocities most com-

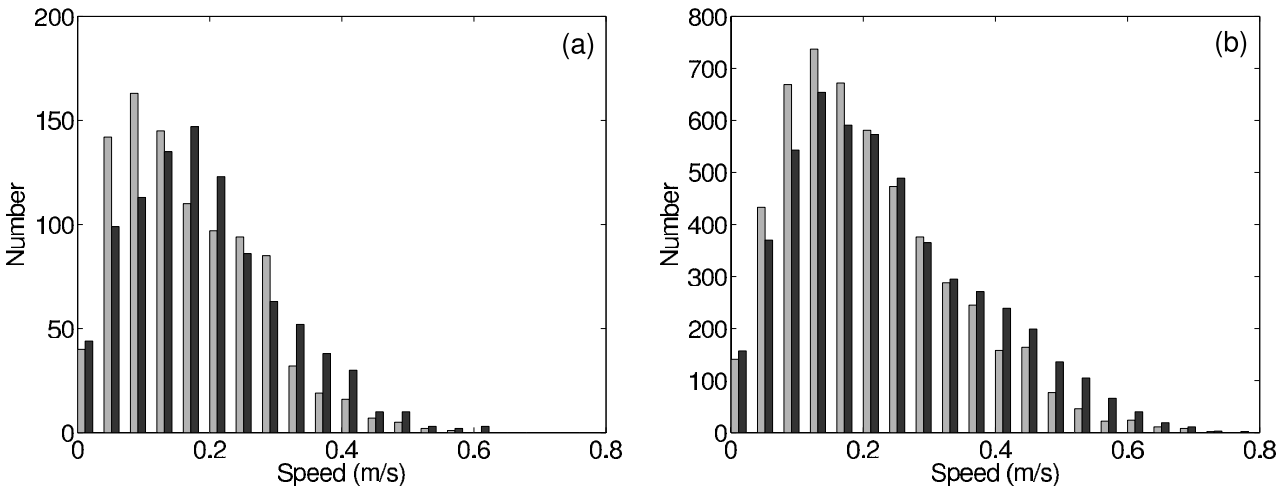

Figure 14. Histograms of current speeds from (a) drifters shown in shading and nearby HF radar data shown in black and (b) 5 m ADCP data from the D130 mooring (shaded) and nearby HF radar data (black).

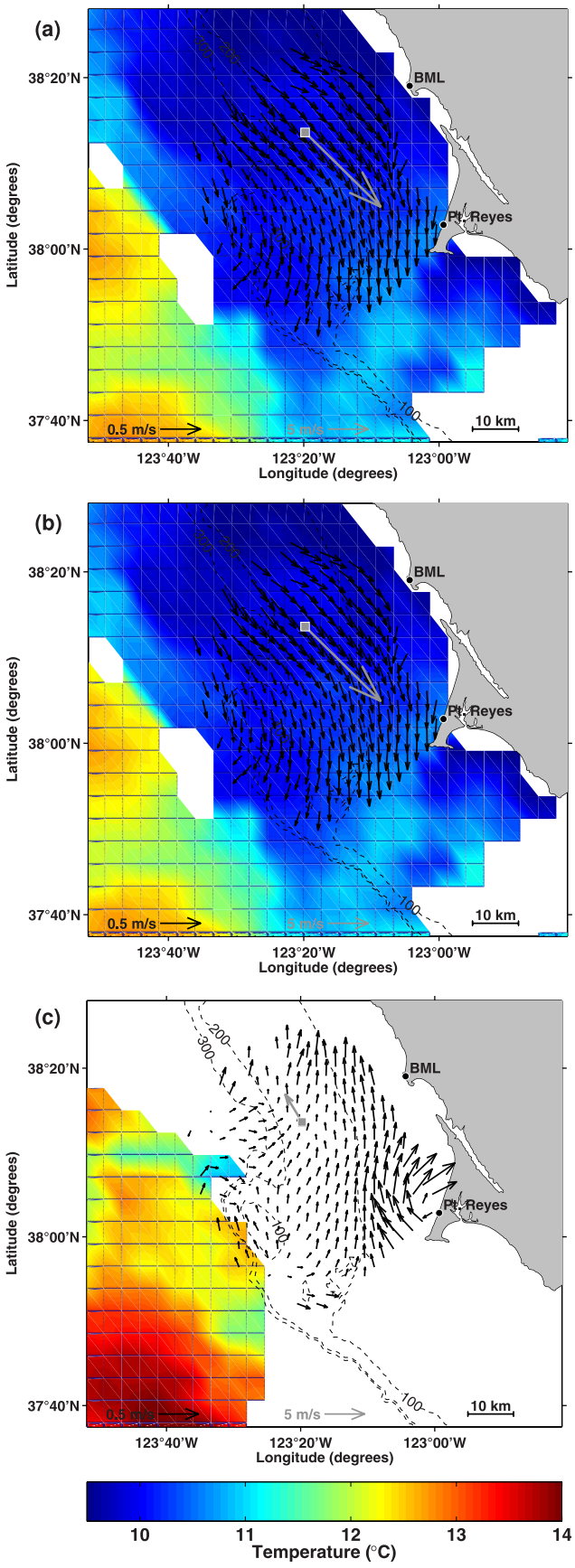

Figure 15. Daily average surface currents overlayed on MODIS Terra Global Level 3 Mapped Thermal IR sea surface temperature (daily; 4.63 km spatial resolution) for (a) 18 May, (b) 19 May, and (c) 21 May of 2001. Shaded arrow indicates daily average wind strength for the same time period from NDBC 46013 winds. The same color scale for temperature data, shown to the right of Figure 15c, was used for all panels. Large area without sea surface temperature (SST) on 21 May (Figure 15c) was due to cloud cover. For visual clarity, only half the HF radar grid points are shown.

monly 0.05–0.15 m/s and radar velocities 0.15–0.25 m/s. A similar trend toward higher radar velocities is seen when HF radar currents are compared with ADCP currents (Figure 14b).

[45] These quasi-Eulerian drifter velocities can also be used to assess the differences between drifter and radar vectors. The RMS velocity difference between radar and drifter currents is 13 cm/s, similar to the values for ADCP data. Cross correlations between complex-valued HF radar currents and drifter currents had a magnitude of 0.76, highly significant. Drifter currents are, on average, not rotated with respect to nearby HF radar currents (complex correlation phase of 0° ± 2°), despite the fact that drifters generally move seaward of radar-derived particle tracks.

5. Wind Band: Subtidal Circulation

[46] Subtidal circulation off northern California is largely in response to local wind forcing [*Beardsley et al.*, 1987; *Winant et al.*, 1987; *Largier et al.*, 1993], although remote wind forcing [*Denbo and Allen*, 1987] and offshore mesoscale forcing [*Largier et al.*, 1993] may also be important. The association between wind and surface current variability has already been demonstrated with cross spectra (Figure 10) and spatial maps of cross correlations (Figures 11c and 11d).

[47] The major benefit of radar data is that one can observe the details of the spatial pattern of surface flow. While it is difficult to show the temporal evolution of this spatial pattern without animation, selected daily average maps of surface current can provide valuable illustrations of many of the flow features commonly observed during upwelling, relaxation, and the transition between these conditions (e.g., Figure 15). Conditions on 18 May 2001 are typical of upwelling (Figure 15a) – winds have been equatorward for a couple of days and surface flow is well organized and strongly equatorward (0.2–0.4 m/s) in response to the wind forcing. There is a noticeable westward deflection of the current immediately upstream of Pt. Reyes. Upwelled cold waters are evident throughout the radar domain. As the winds weaken (19 May 2001), poleward flow develops in the vicinity of Pt. Reyes and inshore along the coast past Bodega Bay, but equatorward flow continues over the outer shelf and the surface temperatures remain low (Figure 15b). Over the next 2 days an unusual poleward wind occurs and poleward flow is observed throughout the radar domain, but with strongest currents over the inner

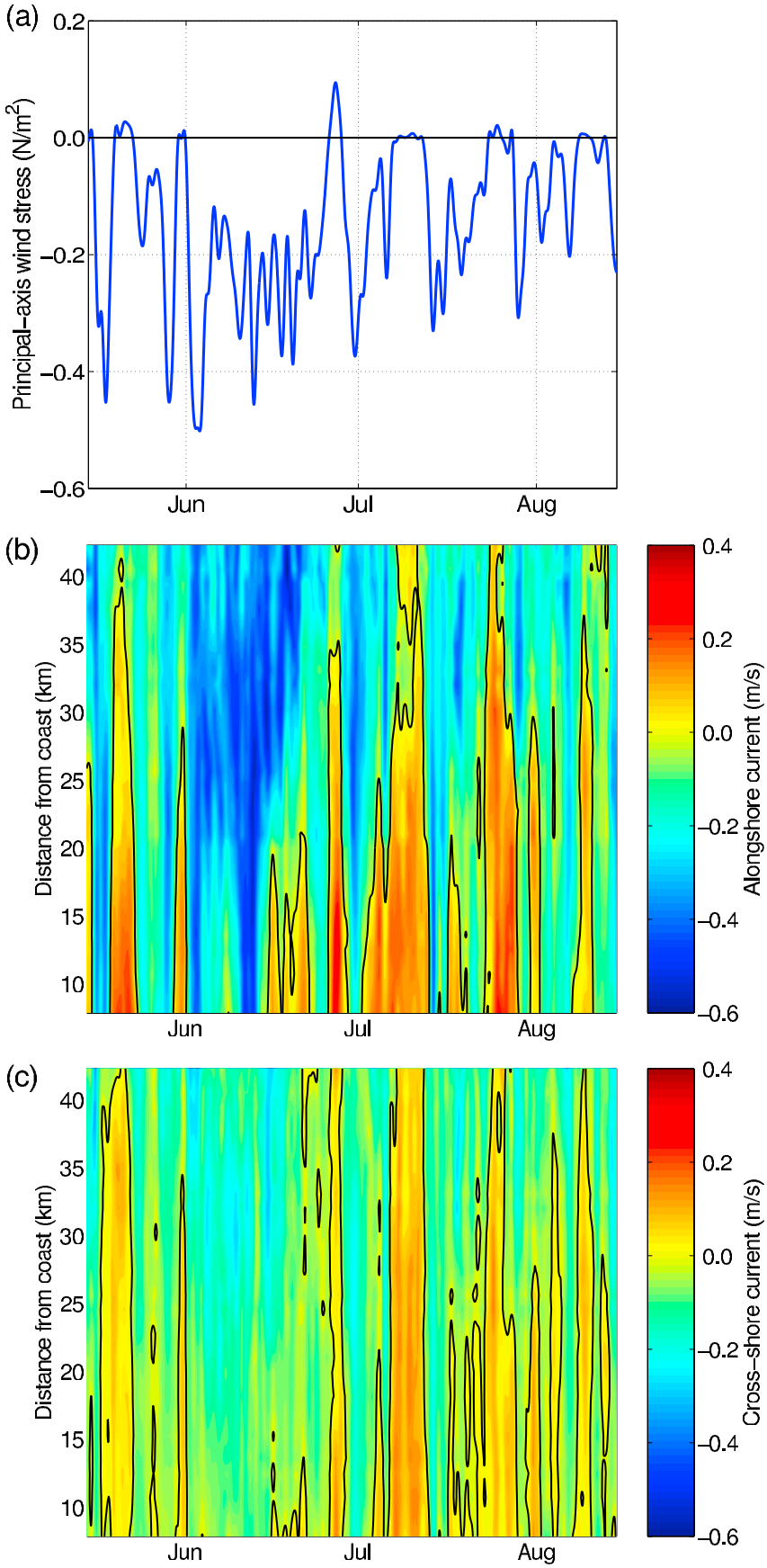
(a)
Principal–axis wind stress (N/m^2)
0.2
0.0
−0.2
−0.4
−0.6
Jun
Jul
Aug
(b)
Distance from coast (km)
40
35
30
25
20
15
10
Jun
Jul
Aug
0.4
0.2
0.0
−0.2
−0.4
−0.6
Alongshore current (m/s)
(c)
Distance from coast (km)
40
35
30
25
20
15
10
Jun
Jul
Aug
0.4
0.2
0.0
−0.2
−0.4
−0.6
Cross–shore current (m/s)

Figure 16

shelf. The strongest currents are observed in the vicinity of Pt. Reyes and a separation vortex is evident immediately north and west of the point (and corroborated by drifters deployed immediately south of the point, 18–19 May). While cloud cover prevents nearshore satellite coverage, these relaxation/poleward flows typically lead to a warming of nearshore temperatures [*Send et al.*, 1987; *Wing et al.*, 1995a, 1995b]. On 21 May, there is also a suggestion of onshore flow of warm offshore waters across the southern boundary of the radar domain.

5.1. D-Line Subtidal Currents

[48] This reversal of equatorward upwelling flows is repeated many times in 2001, during weakening or reversal of the wind forcing. One can see the pulsing of these events and the associated cross-shore structure by plotting the time-dependent flow on the D-line slice of HF radar data (Figure 16). Current fluctuations closely follow changes in the alongshore wind speed, with poleward flow being observed over the shelf whenever winds weakened (Figure 16a). The strongest and most widespread poleward flow events occurred in response to the absence of equatorward winds and/or during weak poleward winds. There are clear cross-shore differences in the response of currents to the wind fluctuations, which are much stronger than the cross-shore structure in wind forcing [*Dever et al.*, 2005; Dorman et al., submitted manuscript, 2005]. Over the inner shelf, alongshore flows are more often poleward than equatorward (cf., Figure 4), with strong equatorward flows being observed on only a handful of occasions during summer 2001 (most notably in early June). Many of the poleward flow events extend no more than 20–25 km offshore, extending over the midshelf. Over the outer shelf and slope, surface flow is strongly and persistently equatorward (e.g., speeds of 0.4–0.5 m/s persist throughout the first 3 weeks of June). Patterns of cross-shore flow exhibit similar structure to the alongshore flow, but are smaller in magnitude.

5.2. Empirical Orthogonal Function (EOF) Analysis

[49] Empirical orthogonal function analysis of subtidal radar flow patterns yielded 3 dominant modes, which together explained 80% of the overall variance. The first EOF explained 67.6% of the variance and represented the predominant alongshore flow pattern that reversed in concert with fluctuations in equatorward wind forcing (Figure 17a). The correlation between the first EOF time series and alongshore wind stress is very high (0.85).

[50] The physical interpretation of the second and third modes is more difficult as these patterns add detail to the uniformity of the first mode, effectively "correcting" it for the observed complex cross-shore and alongshore structure. The second mode appears to represent the cross-shore shear between the poleward flow over the shelf and equatorward further offshore during relaxation events (Figure 17b). However, as can be seen in Figure 16, the cross-shore structure is different during each event and this second EOF mode does not correlate simply with wind stress. This mode accounts for 8.6% of the total variance. The third mode accounts for only 3.9% of the total variance and represents a more complex pattern, dominated by strong flows offshore and an eddy-like connection between these and flows over the shelf. All higher modes explained no more than 2% of the overall variance each.

5.3. Regression of Wind Stress on Radar Data

[51] Linear correlations and linear regression were used to test the relationship between wind forcing and surface currents over the domain of radar data. Maximum lagged linear correlations between wind stress and subtidal surface currents at each grid point show that nearshore there is a small, but consistent lag of currents with respect to the wind (3–6 hours; Figure 18a). Offshore, currents preceded winds measured at the NDBC mooring slightly, suggesting that offshore winds precede shelf winds somewhat.

[52] Linear regressions between principal axis wind stress and principal axis currents at the lags of maximum correlation were highly significant at all grid points. Regression coefficients were of order 1 $m^3/N/s$ (Figure 18b). The region of maximum regression coefficient was west of Bodega Bay and north of Cordell Bank. The current at zero wind stress (y intercept) from the regressions shows a strong cross-shore gradient, with significant poleward current nearshore and strong equatorward flow off the shelf, suggesting a cross-shore structure in the large-scale pressure gradient that presumably generates flow at zero wind forcing (Figure 18c).

6. Tide Band: Tidal, Diurnal, and Inertial Currents

[53] Spectral analysis of HF radar data revealed clear signals at the tidal, diurnal and inertial frequencies (Figures 5 and 9). All of these signals, with the exception of the semidiurnal tidal signal, were dominated by clockwise rotating fluctuations.

6.1. Tidal Analysis

[54] Tidal harmonics explain about 4–15% of the total variance in the complex current and 10–50% of the variance in the tidal/diurnal/inertial band (frequencies greater than 0.7 cpd). The variance contained in tidal harmonics increases along the northern, western and southern extremes of the data region, with the highest values directly north of Pt. Reyes.

[55] Individual tidal constituents exhibit considerable spatial variability (Figure 19). The dominant harmonics

Figure 16. (a) NDBC 46013 alongshore wind stress, (b) D-line alongshore currents, and (c) D-line cross-shore currents during the summer months of 2001. In Figure 16a, wind stress is shown in blue, with negative values indicating equatorward winds. The horizontal black line indicates zero alongshore wind stress. In Figures 16b and 16c the vertical axis is distance from shore along the D-line. Red indicates poleward (Figure 16a) and onshore (Figure 16b) flow typically associated with relaxation, while blue indicates equatorward (Figure 16a) and offshore (Figure 16b) flow. The overlayed black lines on Figures 16b and 16c indicate zero alongshore and cross-shore flow, respectively.

are M_2, K_1, O_1, P_1, and S_2. Other constituents either had low signal-to-noise ratios at the majority of the grid points or accounted for very little of the total tidal energy. Although the eight months of data used to calculate tidal harmonics is theoretically sufficient to distinguish between all of the above constituents, it is not possible to clearly separate either K_1 (1.003 cpd) or P_1 (0.997 cpd) from a true 24 hour signal (diurnal signal; 1 cpd). Similarly, S_2 (2 cpd) cannot be separated from the first harmonic of the true diurnal signal. Further limitations are that this tidal analysis can only identify phase-locked, barotropic tides and will not extract much of the energy in baroclinic (internal) tides which are not phase locked.

[56] Diurnal tidal constituents (K_1, P_1 and O_1) are predominantly clockwise-rotating (Figures 19–19c), consistent with spectral results (Figure 9). A notable exception, however, is the counterclockwise rotation of the O_1 tide in the vicinity of Pt. Reyes. Both the O_1 and K_1 tides are strong over Cordell Bank and around Pt. Reyes, where they exhibit a more linear polarization. Away from Cordell Bank, the O_1 tide showed linear polarization aligned with isobaths, while K_1 and P_1 exhibited more complex spatial patterns in strength and direction. In particular, P_1 tidal ellipses are perpendicular to isobaths near Pt. Reyes.

[57] Semidiurnal tides show a much more complex pattern of rotation, but they are on the whole clockwise over the shelf and counterclockwise over the slope and Cordell Bank. This is particularly true for the M_2 tide, although it also exhibits a reversed polarization near Pt. Reyes (Figure 19d). M_2 tides are strongest over the slope and over Cordell Bank, though there is significant semidiurnal tidal energy near Pt. Reyes. Over the shelf, they are weaker and exhibit nearly linear polarization aligned with the isobaths. S_2 tides are considerably weaker than the other tidal constituents and show more complex spatial patterns of rotation (Figure 19e).

6.2. Diurnal Wind Forcing

[58] Winds also exhibit significant energy at the frequencies of the diurnal tidal constituents K_1 and P_1, suggesting that wind-driven radiational tides could represent an important component of the tidal energy measured in the surface currents at those frequencies. Further, at these tidal frequencies the strength of currents diminishes 25–35% between 5 m and 9 m on the C90 mooring (Figure 9) and tidal ellipses are rotated clockwise with respect to the wind forcing (see wind tidal ellipses shown at bottom right on Figures 19b and 19c). These observations argue that much of the diurnal signal in currents is due to diurnal wind forcing, as previously discussed by *Beardsley et al.* [1987]. Consistent with this is the observation that nearshore tidal ellipses for K_1 and P_1 exhibit notable cross-shore energy (cf., alongshore alignment of the linear polarization of other constituents). Further, correlations of the demodulated signal in diurnal winds and radar currents exhibit significant values (0.25–0.5) in the eastward parts of the radar domain, i.e., over the shelf and within about 20 km of the shore. Correlations are strongest along the inner shelf just off

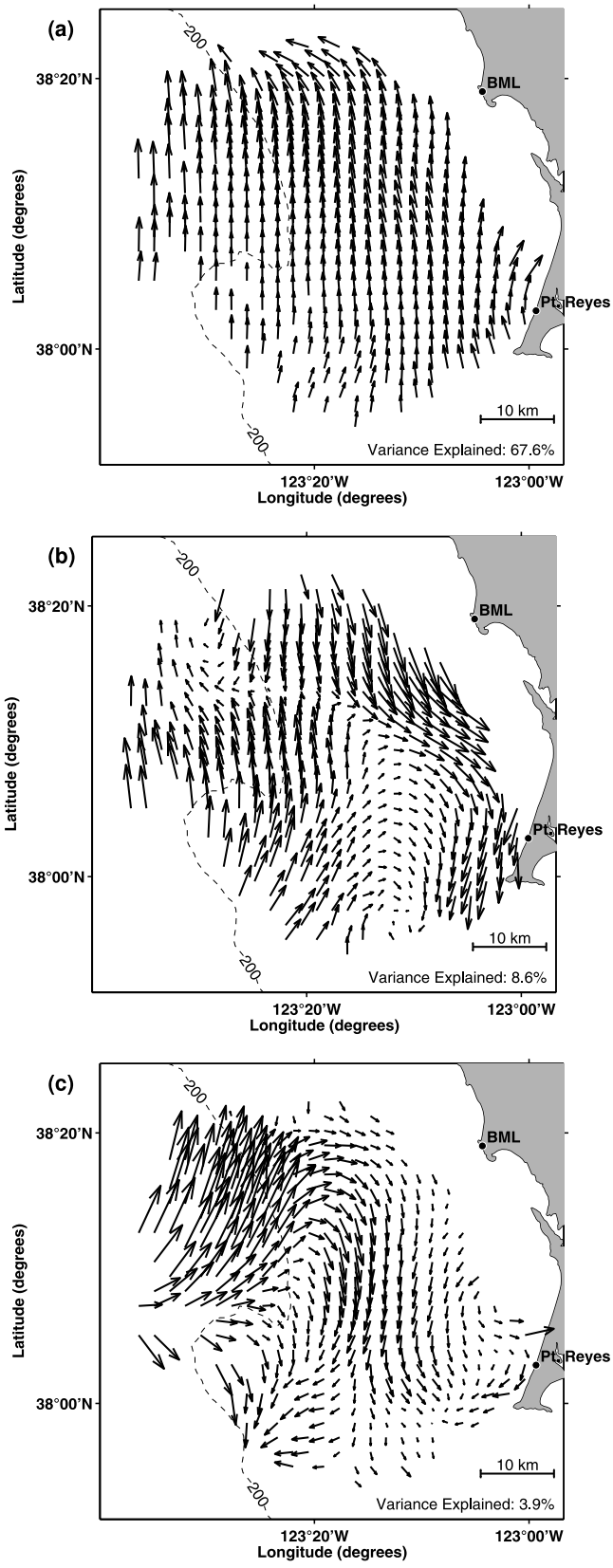

Figure 17. (a) First, (b) second, and (c) third empirical orthogonal functions (EOF) of subtidal current data from June to August of 2001. The first, second, and third EOFs represent 67.6%, 8.6%, and 3.9% of the subtidal variance, respectively. Note that EOFs are all normalized to have unit magnitude, and size of vectors does not represent strength of EOF relative to other EOFs.

Bodega Head. The current signal lags the wind signal by about 0.5 day.

6.3. Inertial Currents

[59] There is a broad peak in radar current variance around the inertial frequency (1.24 cpd at 38° latitude). Fourier spectra exhibit enhanced energy between 1.18 and 1.41 cpd, i.e., periods of 17.0 to 20.4 hours (Figure 9). The center of this band occurs at 1.29 cpd, about 4.3% higher that the true inertial frequency, consistent with the 5% increase noted by *Pollard* [1970] and *Kundu* [1976]. As seen in the rotary spectra (Figure 9), variance in this inertial band is dominated by clockwise rotation. Clockwise-oriented fluctuations (Figure 20) are 5–10 times more energetic than counterclockwise fluctuations (not shown). Near-inertial variance is greatest offshore, specifically toward the north (away from Cordell Bank). There is a marked decrease in near-inertial energy over the inner shelf from about 15 km offshore, consistent with the interaction of inertial motions with the coastal boundary. Wind forcing of inertial motions is equivocal as there is only weak correlation between demodulated signals of wind and surface current (about 0.4). Maximum demodulated correlations between wind and surface currents at the inertial frequency occurred at a lag of about one inertial period.

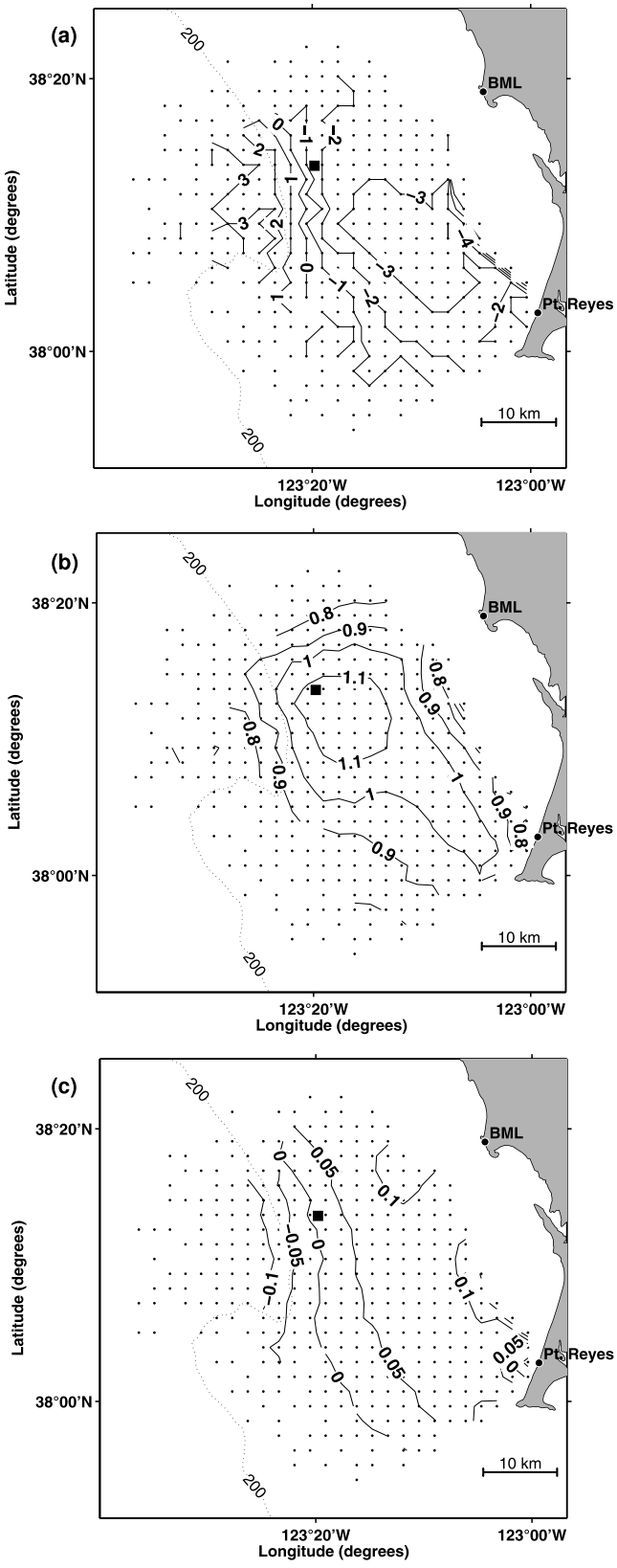

Figure 18. Results of linear regression of alongshore wind stress from NDBC 46013 mooring against principal-axis, subtidal surface currents at each grid point. (a) Lag in hours that produced the maximum correlation between the two time series. Regressions were performed at lag with maximum correlation. (b) Value of the regression coefficient (in $m^3/N/s$), and (c) surface current (in m/s) at zero wind stress derived from the regression. In all panels the location of the NDBC mooring is indicated by a shaded square.

7. Discussion

[60] High-frequency radar data on surface currents provide an unprecedented view of surface circulation in the Reyes-Bodega region, combining high resolution in both the temporal and spatial dimensions. Though there have been a number of important studies of current patterns in this area, radar data have revealed a complexity of flow at a level of detail that was not previously available. In particular, this study has revealed strong cross-shelf structure in coastal circulation, with a tendency for weak or poleward flows nearshore in spite of strong wind forcing in the region. Further, the spatial pattern of surface currents during relaxation is well described, including large eddies and flow complexity observed between poleward flow nearshore and equatorward flow offshore. This work represents a first step toward obtaining a realistic view of the rates and patterns of plankton dispersion in time-variable coastal upwelling regions.

7.1. Evaluation of the Quality of HF Radar Data

[61] Comparison between radar and in situ observations indicates a high degree of agreement between similar measurements. Cross correlations with 5 m ADCP data from the WEST moorings were highly significant near the mooring location (0.7–0.9), although RMS velocity differences were considerable (0.13–0.19 m/s) and HF radar data show higher current speeds than those found in near-surface ADCP data (Figure 14). Comparisons between colocated measurements of drifter-derived velocities and radar current data showed similar levels of correlation and RMS differ-

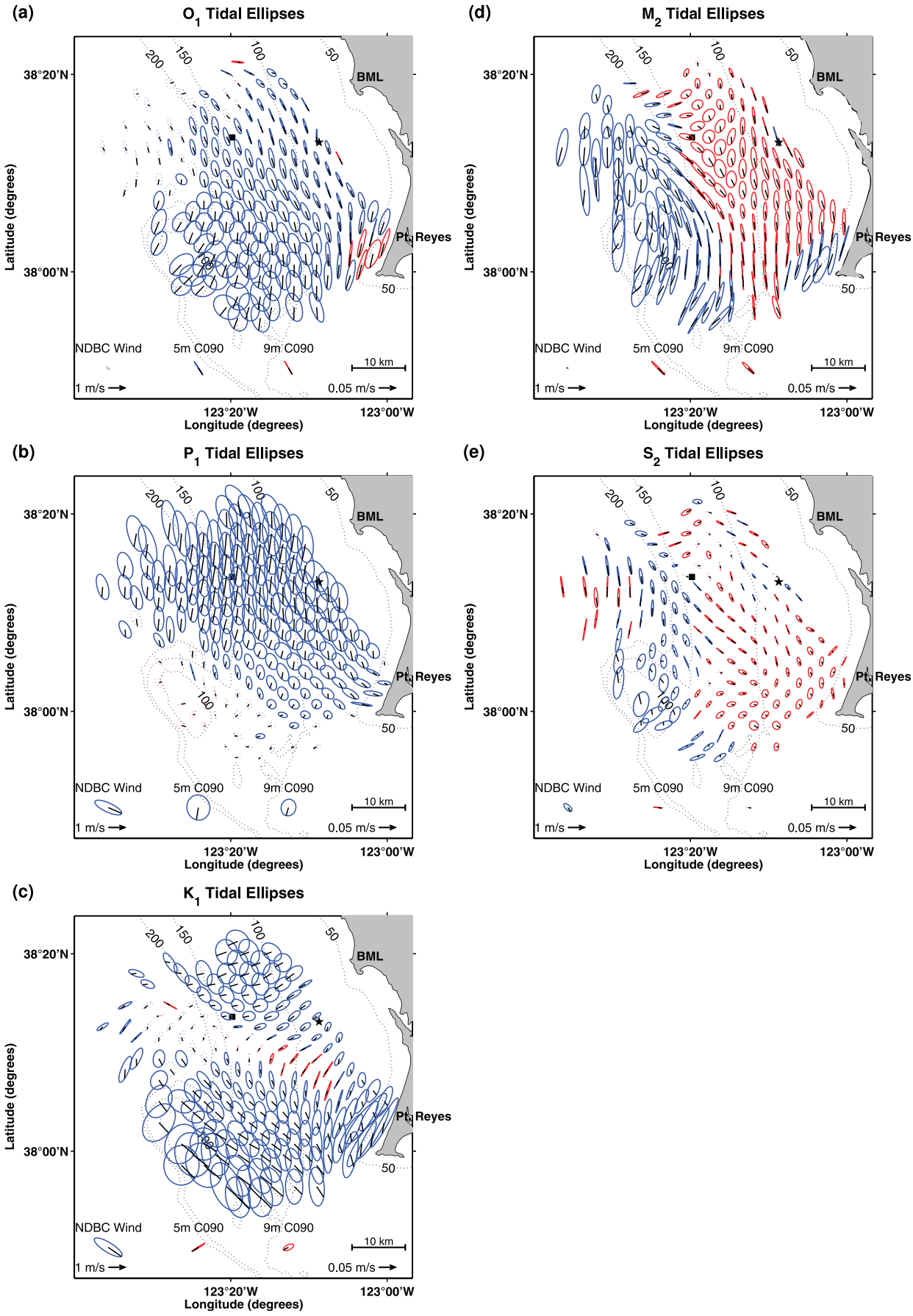
(a)
O1 Tidal Ellipses
(d)
M2 Tidal Ellipses
(b)
P1 Tidal Ellipses
(e)
S2 Tidal Ellipses
(c)
K1 Tidal Ellipses
38°20'N
38°00'N
Latitude (degrees)
123°20'W
123°00'W
Longitude (degrees)
BML
Pt Reyes
200
150
100
50
NDBC Wind
5m C090
9m C090
10 km
1 m/s
0.05 m/s

Figure 19

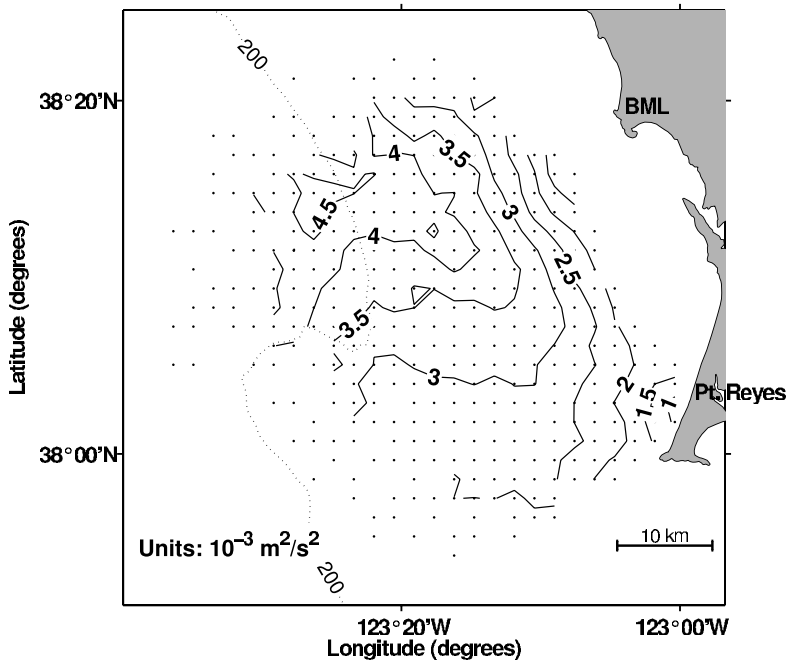

Figure 20. Variance in clockwise-rotating fluctuations contained in inertial band (1.18–1.41 cpd; 17.0–20.4 hours). Contours are in units of 10^{-3} m^2/s^2. Variance in counterclockwise-rotating fluctuations (not shown) was a factor of 10 smaller than that in clockwise-rotating fluctuations.

ences. Drifter and HF radar particle tracks separate at a rate of approximately 5 km/d. This level of discrepancy between drifter and radar measurements is within the range of discrepancies found by other investigators (H. Statscewich, personal communication, 2004; J. D. Paduan, personal communication, 2004).

[62] One can expect differences between HF radar currents and both ADCP and drifter velocities due to several real phenomena, such as horizontal shear with depth, Stokes Drift and the difference between Eulerian and Lagrangian velocities. Measurements along the eastern coast of the United States (Kohut et al., submitted manuscript, 2005) yielded RMS velocity differences between adjacent ADCP current bins of the same order of magnitude as differences between ADCP and HF radar currents separated by a similar depth, suggesting that much of our observed discrepancy between radar and ADCP currents could be due to real differences between current profiles at different depths. Wind-driven forcing at the surface is consistent with the tendency toward higher velocities seen in HF radar surface currents than in subsurface ADCP and drifter currents. Furthermore, most drifter tracks were to the right of radar tracks, consistent with Ekman layer structure and the deeper level of flow observed by drifters (5–10 m). Determining the relative importance of these factors in explaining the overall differences between radar tracks and drifter paths is difficult given the significant intrinsic noise in individual radar current measurements and would most likely require a large number of drifter paths under different current and water column conditions.

7.2. Cross-Shore Structure of Alongshore Flow

[63] The classical view of wind-driven upwelling has strong equatorward alongshore currents over the shelf in response to a cross-shelf barotropic pressure gradient due to offshore Ekman transport. Although previous studies have described shear in this alongshore flow, including the possibility for poleward flow nearshore during relaxation [*Largier et al.*, 1993], the cross-shelf structure of this alongshore flow has not been well described. To date, attention has remained on the time dependence of this flow. In Figure 4, however, there is a marked cross-shelf structure to this alongshore flow. Three regions can be identified: (1) nearshore, within 15 km of the shoreline, where both the mean and the mode of alongshore currents are poleward, and where current speeds rarely exceed 0.25 m/s in either direction; (2) inner shelf, between 15 and 25 km offshore, where currents are typically equatorward, but weak, often

Figure 19. Tidal ellipses at (a) O_1, (b) P_1, (c) K_1, (d) M_2, and (e) S_2 frequencies. Clockwise rotating ellipses are shown in blue, and counterclockwise ellipses are in red. Black lines emanating from the center of each ellipse denote flow direction at the time of greatest tidal flow in that harmonic from ADCP data at 9 m on the C090 mooring. For clarity, only half the HF radar grid points are shown, and tidal ellipses from NDBC wind data (the location of which is indicated by a black square) and 5 m and 9 m ADCP data from C090 (indicated by a black, five-point star) are shown at the bottom of each panel. Dashed lines are used for tidal ellipses that have a signal-to-noise ratio less than 2.

less than 0.1 m/s; and (3) outer shelf, between 25 and 45 km offshore, where both the mean and the mode of alongshore currents are equatorward and strong, about 0.25 m/s. Over the inner and midshelf (10 to 25 km offshore), there is a transition to stronger equatorward currents with distance offshore, but beyond 25 km maximum currents remain at about 0.5 m/s. Offshore of 45 km, strong alongshore currents are less common and poleward currents are again present, presumably in association with offshore mesoscale features.

[64] This marked structure reflects cross-shelf patterns in forcing. Dorman et al. (submitted manuscript, 2005) and A. Kochanski and D. Koracin (Comparison of wind stress algorithms and their influence on wind stress curl using buoy measurements over the shelf of Bodega Bay, California, submitted to *Deep-Sea Research, Part II*, 2005) describe wind patterns with significant curl and weaker equatorward forcing over the inner and midshelf at times. However, beyond weaker winds and increased frictional drag in shallower waters, this structure points to significant pressure gradients that can account for poleward flows. For example, regressions between wind stress and surface currents (Figure 18) indicates that an equatorward wind stress of order 0.05 N/m^2 may be required to counter poleward forcing and produce zero surface current over the midshelf, but not over the outer shelf. While the presence of poleward pressure forcing has been noted by *Largier et al.* [1993] and *Gan and Allen* [2002] for this region, poleward surface currents are very rare between 30 and 40 km offshore and there is little indication of poleward flow in the absence of equatorward wind forcing. This may be due to offshore forcing of the outer shelf by the main flow of the California Current. In addition to large-scale barotropic pressure gradients, the small scale of the coherent patterns in shear suggests that spatially complex baroclinic pressure gradients may be set up by the spatially complex wind field (i.e., patterns in wind curl). Further, small-scale barotropic pressure gradients may develop along the upstream edge of Point Reyes, slowing and diverting alongshelf flow in the Bodega region – this is consistent with weaker equatorward flow over the midshelf and increased offshore flow over the outer shelf (Figure 4). Strong equatorward flows over the outer shelf may be partly due to strong flows that are generated by wind forcing further north and that separate from the coast prior to reaching the Bodega Bay area.

[65] This cross-shelf shear in alongshelf flows is key to the distribution of water-borne material in the region, with nearshore poleward flows importing warm plankton-rich waters from the Gulf of Farallones, midshelf equatorward flows bringing cold newly upwelled waters south from Point Arena, and outer shelf equatorward flows importing offshore California Current surface water. Future work is directed at linking this complex pattern of advection to the notable structure observed in plankton and water property distributions during research cruises in this region [*Kaplan and Largier*, 2005]. In the presence of this strong shear, cross-stream mixing, due to small-scale motions such as tides and inertial motions, will be very effective in bringing about alongshore shear dispersion.

[66] Although this structure may be particularly well developed off Bodega, reports of poleward flow over the inner shelf in other upwelling locations [*Relvas and Barton*, 2005] suggests that this cross-shelf structure in alongshelf flow may be a common feature in coastal upwelling and that it deserves further attention in terms of both causes and consequences.

7.3. Upwelling-Relaxation Cycle

[67] The temporal variability in shelf currents is well recognized and correlation with wind forcing indicates that this is primarily in response to fluctuations in wind forcing [e.g., *Winant et al.*, 1987; *Largier et al.*, 1993]. This correlation is strong over the whole radar domain (Figure 18) and wind-correlated currents account for 2/3 of the observed subtidal variability. However, the response to wind variability is not uniform. The poleward flows over the inner shelf extend over much of the shelf during periods of weaker upwelling winds, but they only extend out over the outer shelf (and weakly) at times when the upwelling winds disappear for several days.

[68] The temporal fluctuations in currents are not uniform and this results in shear, specifically between poleward flows over the inner and midshelf and equatorward flows over the outer shelf and slope. The resultant complexity in flow patterns, including a recurrent anticyclonic eddy, is reflected in the second and third EOF modes (Figure 17), which account for 1/8 of the variance in surface currents.

[69] Small-scale flow patterns are also evident nearshore. Most notably, a strong clockwise eddy is observed on the northwest side of Point Reyes during poleward flow past the point. This separation eddy is strong enough to trap and beach drifters moving north past the Point and it indicates the strength of poleward flow at the Point. This strong current and eddy in the vicinity of Point Reyes during periods of wind relaxations also suggests a connection with areas to the south of the Point, including the possibility of transport and deposition of biotic and abiotic materials.

7.4. Patterns of Tidal and Inertial Energy and Diurnal Winds

[70] The power levels and clockwise polarization of the HF radar spectra are in good agreement with the results of *Paduan and Rosenfeld* [1996]. Diurnal wind forcing is evident in the high wind-radar coherences at the diurnal frequency and the cross-isobath orientation of nearshore P_1 tidal ellipses. In contrast, inertial currents are weaker nearshore, as expected, and almost completely circularly polarized in the clockwise direction offshore.

[71] The change in polarization of the M_2 tidal ellipses at the shelf break is consistent with the propagation of internal tidal waves away from the shelf break, in both directions. *Paduan and Cook* [1997] have similarly attributed patterns of M_2 tidal ellipse strength and orientation to internal tidal waves. This horizontal structure in tidal currents and orientation could have important consequences for particle transport through small-scale shear dispersion.

[72] M_2 tidal currents are strong and alongshore-polarized in the vicinity of Point Reyes. Furthermore, the change in direction of rotation near the point suggests the reflection of tidal energy from the land mass. Overall increase in tidal energy for all constituents, as well as the increase in subtidal energy, in the vicinity of Pt. Reyes indicates that Pt. Reyes

is indeed an important restriction for coastal currents in the region.

7.5. Lagrangian Trajectories and Dispersion of Plankton

[73] The presence of both poleward and equatorward flows over the shelf is important in terms of alongshore dispersal of plankton. This has consequences for the fate of primary production as well as for the structure of metapopulations of benthic invertebrates and reef fish. Strong cross-shore gradients in alongshore flow patterns indicate that relatively nearby water masses could experience significantly different transport patterns. The potential for shear dispersion is high [*Largier*, 2004]. On the other hand, persistent poleward flow over the inner shelf despite strong equatorward flows elsewhere suggests a mechanism for local retention of plankton. Through control on cross-shore position, perhaps achieved through vertical migration at appropriate times, plankton could assert strong influence on alongshore transport.

[74] In future work, we hope to explore in more detail surface water transport patterns. We believe that understanding these coastal flow patterns is essential to explaining patterns of primary productivity and meroplankton dispersal in this and other upwelling regions. HF radar surface currents, with its high spatial and temporal resolutions, will undoubtedly be invaluable in these efforts.

8. Conclusions

[75] The initial eight months of HF radar data from the Bodega-Reyes region has been described and analyzed in detail. Comparison with subsurface ADCP currents and drifter tracks provide a high level of confidence in the observed surface flow patterns. The primary insights offered in this paper are based on the spatial extent and density of this data, as well as its high temporal resolution. In addition to expected flow features associated with a headland like Pt. Reyes and tight wind-current coupling, surface currents reveal strong cross-shelf structure in the mean and variability of alongshore currents. Significant organized cross-shore structure is present in both high-frequency tidal band fluctuations and in subtidal, wind-driven circulation. In particular, currents over the mid- and inner shelf are predominantly weak or poleward, and an important coastal jet of poleward flow develops within 20 km of the coast north of Pt. Reyes during periods of relaxation in wind forcing. This complex cross-shore structure has not been fully described previously. It is reasonable to expect that similar structures would be observed in other upwelling systems and that the results shown here provide more general insight into the functioning of eastern boundary systems. Furthermore, this structure in alongshore flow is of central importance to quantifying and understanding alongshore transport and dispersion of plankton in coastal upwelling regions [e.g., *Kaplan and Largier*, 2005].

[76] **Acknowledgments.** We would like to thank Clive Dorman for help with the wind data, Raphael Kudela for providing AVHRR images, and Ed Dever for the moored ADCP and temperature data. Further, we acknowledge the assistance and useful suggestions of Jeff Paduan, Mike Cook, Mike Kosro, Belinda Lipa, and Bruce Nyden. This work has been funded by NSF CoOP Project grant OCE-9907884 and the Sonoma County Water Agency. Contribution number 2267, Bodega Marine Laboratory, University of California.

References

Barrick, D. E., and B. Lipa (1986), An evaluation of least-squares and closed-form dual-angle methods for CODAR surface-current applications, *IEEE J. Oceanic Eng.*, *11*, 322–326.

Barrick, D. E., and B. Lipa (1999), Using antenna patterns to improve the quality of SeaSonde HF radar surface current maps, in *Proceedings of the IEEE Sixth Working Conference on Current Measurement*, edited by S. P. Anderson et al., pp. 5–8, Inst. of Electr. and Electr. Eng., Piscataway, N. J.

Barrick, D. E., J. M. Headrick, R. W. Bogle, and D. D. Crombie (1974), Sea backscatter at HF: Interpretation and utilization of the echo, *Proc. IEEE*, *62*, 673–680.

Beardsley, R. C., and S. Lentz (1987), The Coastal Ocean Dynamics Experiment collection: An introduction, *J. Geophys. Res.*, *92*, 1455–1463.

Beardsley, R., R. Limeburner, and L. Rosenfeld (1985), CODE-2: Moored array and large-scale data report, *Tech. Rep. WHOI-85-35*, 21 pp., Woods Hole Oceanogr. Inst., Woods Hole, Mass.

Beardsley, R. C., C. E. Dorman, C. A. Friehe, L. K. Rosenfeld, and C. D. Winant (1987), Local atmospheric forcing during the Coastal Ocean Dynamics Experiment: 1. A description of the marine boundary layer and atmospheric conditions over a northern California upwelling region, *J. Geophys. Res.*, *92*, 1467–1488.

Bennett, J. R., and H. Clites (1987), Accuracy of trajectory calculation in a finite-difference circulation model, *J. Comput. Phys.*, *68*, 272–282.

Bray, N. A., and C. L. Greengrove (1993), Circulation over the shelf and slope off northern California, *J. Geophys. Res.*, *98*, 18,119–18,145.

Brink, K. H., and T. J. Cowles (1991), The Coastal Transition Zone program, *J. Geophys. Res.*, *96*, 14,637–14,647.

Chapman, R. D., and H. C. Graber (1997), Validation of HF radar measurements, *Oceanography*, *10*, 76–79.

Crosby, D. S., L. C. Breaker, and W. H. Gemmill (1993), A proposed definition for vector correlation in geophysics: Theory and application, *J. Atmos. Oceanic Technol.*, *10*, 355–367.

Davis, R. (1985), Drifter observations of coastal surface currents during CODE: The method and descriptive view, *J. Geophys. Res.*, *90*, 4741–4755.

Denbo, D. W., and J. S. Allen (1987), Large-scale response to atmospheric forcing of shelf currents and coastal sea level off the west coast of North America: May–July 1981 and 1982, *J. Geophys. Res.*, *92*, 1757–1782.

Dever, E. P. (1997a), Subtidal velocity correlation scales on the northern California shelf, *J. Geophys. Res.*, *102*, 8555–8571.

Dever, E. P. (1997b), Wind-forced cross-shelf circulation on the northern California shelf, *J. Phys. Oceanogr.*, *27*, 1566–1580.

Dever, E. P., C. E. Dorman, and J. L. Largier (2005), Surface boundary layer variability off northern California, USA during upwelling, *Deep Sea Res., Part II*, in press.

Dorman, C. E., and C. D. Winant (1995), Buoy observations of the atmosphere along the west coast of the United States, 1981–1990, *J. Geophys. Res.*, *100*, 16,029–16,044.

Gan, J. P., and J. S. Allen (2002), A modeling study of shelf circulation off northern California in the region of the Coastal Ocean Dynamics Experiment: Response to relaxation of upwelling winds, *J. Geophys. Res.*, *107*(C9), 3123, doi:10.1029/2000JC000768.

Gaylord, B., and S. D. Gaines (2000), Temperature or transport? Range limits in marine species mediated solely by flow, *Am. Nat.*, *155*, 769–789.

Gonella, J. (1972), A rotary-component method for analyzing meteorological and oceanographic vector time series, *Deep Sea Res., Part II*, *19*, 833–846.

Huyer, A., and P. M. Kosro (1987), Mesoscale surveys over the shelf and slope in the upwelling region near Point Arena, California, *J. Geophys. Res.*, *92*, 1655–1681.

Kaplan, D. M., and J. L. Largier (2005), HF-radar-derived origin and destination of surface waters flowing past Bodega Bay, California, *Deep Sea Res., Part II*, in press.

Kohut, J., and S. Glenn (2003), Calibration of HF radar surface current measurements using measured antenna beam patterns, *J. Atmos. Oceanic Technol.*, *20*, 1303–1316.

Kosro, P. M. (1987), Structure of the coastal current field off northern California during the Coastal Ocean Dynamics Experiment, *J. Geophys. Res.*, *92*, 1637–1654.

Kundu, P. (1976), An analysis of inertial oscillations observed near Oregon coast, *J. Phys. Oceanogr.*, *6*, 879–893.

Large, W. G., and S. Pond (1981), Open ocean momentum flux measurements in moderate to strong winds, *J. Phys. Oceanogr.*, *11*, 324–336.

Largier, J. L. (2003), Considerations in estimating larval dispersal distances from oceanographic data, *Ecol. Appl.*, *13*, 71–89.
Largier, J. L. (2004), The importance of retention zones in the dispersal of larvae, in *Aquatic Protect Areas as Fisheries Management Tools*, edited by J. B. Shipley, pp. 105–122, Am. Fish. Soc., Bethesda, Md.
Largier, J. L., B. A. Magnell, and C. Winant (1993), Subtidal circulation over the northern California shelf, *J. Geophys. Res.*, *98*, 18,147–18,179.
Lentz, S. J. (1994), Current dynamics over the northern California inner shelf, *J. Phys. Oceanogr.*, *24*, 2461–2478.
Lipa, B. J. (2003), Uncertainties in SeaSonde current velocities, in *Proceedings of the IEE/OES Seventh Working Conference on Current Measurement Technology*, pp. 95–100, Inst. of Electr. and Electr. Eng., San Diego, Calif.
Lipa, B. J., and D. Barrick (1983), Least squares methods for the extraction of surface currents from CODAR crossed-loop data: Application at ARSLOE, *IEEE J. Oceanic Eng.*, *8*, 226–253.
Mace, A. J. (2005), Larval accumulation in the lee of a small headland: Implications for marine reserves in an upwelling region, Ph.D. dissertation, Univ. of Calif., Davis.
Paduan, J. D., and M. S. Cook (1997), Mapping surface currents in Monterey Bay with CODAR-type HF radar, *Oceanography*, *10*, 49–52.
Paduan, J. D., and H. C. Graber (1997), Introduction to high-frequency radar: Reality and myth, *Oceanography*, *10*, 36–39.
Paduan, J. D., and L. Rosenfeld (1996), Remotely sensed surface currents in Monterey Bay from shore-based HF radar (Coastal Ocean Dynamics Application Radar), *J. Geophys. Res.*, *101*, 20,669–20,686.
Paduan, J. D., D. E. Barrick, D. Fernandez, Z. Hallock, and C. Teague (2001), Improving the accuracy of coastal HF radar current mapping, *Hydro Int.*, *5*, 26–29.
Paduan, J. D., K. C. Kim, M. S. Cook, and F. P. Chavez (2005), Calibration and validation of direction-finding high-frequency radar ocean surface current observations, *IEEE J. Oceanic Eng.*, in press.
Pawlowicz, R., B. Beardsley, and S. Lentz (2002), Classical tidal harmonic analysis including error estimates in MATLAB using T-TIDE, *Comput. Geosci.*, *28*, 929–937.
Percival, D. B., and A. T. Walden (1993), *Spectral Analysis for Physical Applications: Multitaper and Conventional Univariate Techniques*, 583 pp., Cambridge Univ. Press, New York.
Pollard, R. (1970), On the generation by winds of inertial waves in the ocean, *Deep Sea Res., Part II*, *17*, 795–812.
Prandle, D. (1991), A new view of near-shore dynamics based on observations from HF radar, *Prog. Oceanogr.*, *27*, 403–438.
Preisendorfer, R. W., and C. D. Mobley (1988), *Principal Component Analysis in Meteorology and Oceanography*, vol. 17, Elsevier, New York.
Relvas, P., and E. D. Barton (2005), A separated jet and coastal counterflow during upwelling relaxation off Cape Sao Vicente (Iberian Peninsula), *Cont. Shelf Res.*, *25*, 29–49.
Send, U., R. C. Beardsley, and C. Winant (1987), Relaxation from upwelling in the Coastal Ocean Dynamics Experiment, *J. Geophys. Res.*, *92*, 1683–1698.
Shumway, R. H., and D. S. Stoffer (2000), *Time Series Analysis and Its Applications*, 549 pp., Springer, New York.
Stewart, R. H., and J. W. Joy (1974), HF radio measurements of surface currents, *Deep Sea Res.*, *21*, 1039–1049.
Strub, P. T., J. S. Allen, A. Huyer, R. L. Smith, and R. Beardsley (1987), Seasonal cycles of currents, temperatures, winds and sea level over the northeast Pacific continental shelf: 35°N to 48°N, *J. Geophys. Res.*, *92*, 1507–1526.
Thomson, D. (1982), Spectrum estimation and harmonic analysis, *Proc. IEEE*, *70*, 1055–1096.
Trowbridge, J. H., and S. J. Lentz (1998), Dynamics of the bottom boundary layer on the northern California shelf, *J. Phys. Oceanogr.*, *28*, 2075–2093.
Washburn, L., D. C. Kadko, B. H. Jones, T. Hayward, P. M. Kosro, T. P. Stanton, S. Ramp, and T. Cowles (1991), Water mass subduction and the transport of phytoplankton in a coastal upwelling system, *J. Geophys. Res.*, *96*, 14,927–14,945.
Wells, D., and N. Beck (1987), *Guide to GPS Positioning*, 2nd ed., Can. GPS Assoc., Fredericton.
Winant, C. D., R. C. Beardsley, and R. E. Davis (1987), Moored wind, temperature, and current observations made during Coastal Ocean Dynamics Experiments 1 and 2 over the northern California continental shelf and upper slope, *J. Geophys. Res.*, *92*, 1569–1604.
Wing, S. R., J. L. Largier, L. W. Botsford, and J. F. Quinn (1995a), Settlement and transport of benthic invertebrates in an intermittent upwelling region, *Limnol. Oceanogr.*, *40*, 316–329.
Wing, S. R., L. W. Botsford, J. L. Largier, and L. E. Morgan (1995b), Spatial structure of relaxation events and crab settlement in the northern California upwelling system, *Mar. Ecol. Prog. Ser.*, *128*, 199–211.
Wing, S. R., L. W. Botsford, and J. F. Quinn (1998a), The impact of coastal circulation on the spatial distribution of invertebrate recruitment, with implications for management, *Can. Spec. Publ. Fish. Aquat. Sci.*, *125*, 285–294.
Wing, S. R., L. W. Botsford, S. V. Ralston, and J. L. Largier (1998b), Meroplanktonic distribution and circulation in a coastal retention zone of the northern California upwelling system, *Limnol. Oceanogr.*, *43*, 1710–1721.

L. W. Botsford and D. M. Kaplan, Wildlife, Fish and Conservation Biology, University of California, Davis, 1 Shields Avenue, Davis, CA 95616, USA. (lwbotsford@ucdavis.edu; dmkaplan@ucdavis.edu)
J. Largier, Bodega Marine Laboratory, University of California, Davis, P.O. Box 247, Bodega, CA 94923, USA. (jlargier@ucdavis.edu)